A Calculation Method for the Three-Dimensional Boundary-Layer Equations in Integral Form

by

Bilal Hafeez Mughal

B.S. University of Virginia (1990)

SUBMITTED TO THE DEPARTMENT OF
AERONAUTICS AND ASTRONAUTICS
IN PARTIAL FULFILLMENT OF THE REQUIREMENTS
FOR THE DEGREE OF

Master of Science
at the
Massachusetts Institute of Technology

September 1992

Signature of Author ______________________________
Department of Aeronautics and Astronautics
August 7, 1992

Certified by ______________________________
Associate Professor Mark Drela
Thesis Supervisor, Department of Aeronautics and Astronautics

Accepted by ______________________________
Professor Harold Y. Wachman
Chairman, Department Graduate Committee

A Calculation Method for the Three-Dimensional Boundary-Layer Equations in Integral Form

by

Bilal Hafeez Mughal

Submitted to the Department of Aeronautics and Astronautics
on August 15, 1992
in partial fulfillment of the requirements for the degree of
Master of Science in Aeronautics and Astronautics

A new numerical method is developed to solve the three-dimensional compressible boundary-layer equations, in integral form, on non-orthogonal grids. The finite-volume scheme employed eliminates the need to compute metric-gradient terms found in curvilinear-coordinate finite-difference methods. The integral method is based on two equations for momentum and one for kinetic energy with empirical equilibrium turbulent-flow closure relations selectively extracted from the literature. Johnston's model is used for the crossflow. The discrete equations are solved simultaneously using the Newton-Raphson method along a row of cells and the solution is marched successively downstream. Spurious saw-tooth modes are kept in check by weighting nodal components in the evaluation of the discrete source terms to augment the Jacobian-matrix diagonal dominance and by applying zero-curvature boundary conditions. Results are computed for a well-known infinite swept wing case to evaluate empirical-closure accuracy, and for a finite swept wing case to demonstrate the full three-dimensional capability.

Thesis Supervisor: Mark Drela,
Associate Professor of Aeronautics and Astronautics

Acknowledgements

I'd like to acknowledge my advisor's insightful and generous guidance throughout this work and his singular accessibility at the shortest notice and the oddest time. I am looking forward to continuing this project under him.

I appreciate the company of my colleagues at the CFDL. In particular, hats off to Brian for his general alacrity in discussion, his comments on this thesis and for generating the Full Potential solution used in Chapter 5. Thanks, also, to two office mates, Tom and Phil, for tolerating my pseudo-wit.

Thanks to Alexandra for her patient proof reading of this document. All remaining split infinitives are my fault.

Finally, I'd like to recognize the extraordinary perseverance and unflinching support of my family throughout a protracted absence from home. They occupy my thoughts as I conclude this Masters work.

This research was supported by Boeing under the supervision of Dr. Wen-Huei Jou.

Contents

List of Figures

Nomenclature

List of Symbols

A	crossflow parameter
B	characteristic matrix
$c_{D_{()}}$	coefficient of dissipation
$c_{f_{()}}$	skin friction
D	dissipation or shear-work integral
$E_{()()}$	components of $\theta^*_{()}$
F_c	compressibility factor
$H_{()}$	shape factor
j	grid counter
$M_{()}$	Mach number
p	pressure
q	speed
$\mathbb{R}$	vector of residuals
$Re_{()}$	Reynolds number
S	cell area
s, n	streamline coordinates
T	matrix of eigenvectors of B
$\boldsymbol{U}$	vector of primary variables
u, v, w	velocity components
$\boldsymbol{W}$	vector of characteristic variables
x, y, z	Cartesian coordinates
α	generic angle
β	angle between external-flow streamline and considered streamline
γ	angle between external-flow streamline and characteristic line
δ	displacement thickness
$\delta^*_{()}$	orientation-dependent displacement thickness
$\delta^{**}_{()}$	orientation-dependent density thickness

η	source-term weighting control along x
θ_ρ	auxiliary density thickness
$\theta_{()()}$	orientation-dependent momentum thickness
$\theta^*_{()}$	orientation-dependent kinetic-energy thickness
λ	source-term weighting control along z
Λ	diagonal matrix of eigenvalues of B
μ	laminar viscosity
ρ	density
τ	shear stress

Subscripts and Superscripts

$()_w$	value at wall
$()_e$	value at boundary-layer edge
$\overline{()}$	meanflow component, incompressible variable, etc.
$()'$	fluctuating component, etc.
$\tilde{()}$	mass-weighted variable
$()^+$	wall-scaled variable

Chapter 1

Introduction

There have been astonishing advances, over the last several years, in the development of Navier-Stokes solvers capable of generating solutions over realistic aircraft configurations. The generation of each solution requires, however, the expenditure of considerable resources, both in terms of hardware and run times, and their routine use, especially by aircraft designers, is still not feasible. To satiate the need for fast, workstation-based solvers, it is, then, only natural to assume one more level of approximation: coupled Euler/boundary-layer or Potential/boundary-layer methods. Not surprisingly, these methods do not significantly reduce accuracy given the considerable empiricism built into Navier-Stokes solvers for turbulent flow. It is with a view to contributing to the viscous aspect of this demand through a coupled approach that this project is undertaken.

Considerable progress has been achieved in the computation of two-dimensional boundary-layer flow and many research forays into three-dimensional flow draw heavily from this experience. This thesis is no exception.

The prediction of three-dimensional turbulent boundary layer flows has only recently begun to garner enough attention, unlike their two-dimensional counterparts, to match their ubiquitous presence in nature. One obvious reason for this historical reticence has been the sheer complexity of general extensions into a third dimension. In addition, for the case of turbulent flow, prediction is still largely an empirical exercise. Therefore, fundamental physical issues continue to strongly motivate current research efforts. In practice, the intrinsic empiricism in turbulent flow prediction has thwarted many efforts at sophisticated modelling of other relevant physics. The present thesis, therefore, attempts to keep the modeling simple while awaiting the ultimate three-dimensional turbulence model.

The ability to handle non-orthogonal grids is crucial in aircraft design. In the usual finite-difference curvilinear approach, cumbersome metrical terms have to be evaluated. The main focus of this thesis is the attempt to apply finite-volume discretization in order to pose the computational problem in a simple locally-Cartesian form, without any additional metric-gradient terms.

The desire to develop a fast scheme suggests the use of an integral form of the equations instead of the more fundamental differential form. This choice is reinforced by the fact that interest is largely confined to the computation of integral quantities. The disadvantage is in the increased reliance on empiricism. In reality, however, integral methods have historically produced results of comparable accuracy to those generated by differential schemes. The gain is an order-of-magnitude increase in speed. Integral schemes also tend to be more robust and are better suited for viscous/inviscid calculations.

This thesis contains the description of a novel compressible, turbulent, integral boundary-layer prediction method on non-orthogonal grids called OMAR (to preempt the inevitable query, the title is not an acronym; in fact, it means nothing). Chapter 2 contains a derivation of the boundary layer equations in an integral form. The necessary closure for turbulent flow is introduced in Chapter 3. Details of the numerical scheme, including finite-volume discretization and the solution method are provided in Chapter 4. The results from two computations, one for a famous infinite swept wing experiment and another for a fully three-dimensional compressible flow over a finite wing, are presented in Chapter 5. In Chapter 6, some suggestions for future work conclude the thesis.

Chapter 2

Governing Equations

2.1 Differential Form

This section contains a brief outline of the derivation of equations in the form that will be used in § 2.2 for integration starting from the more general Navier-Stokes equations. This thesis is concerned only with the steady flow of Newtonian fluids.

The steady compressible boundary-layer equations are obtained from the Navier-Stokes equations by neglecting the effects of transverse pressure variation and diffusion in the streamwise and crosswise directions. In three dimensions, these assumptions leave the equation for mass conservation unchanged,

$$\frac{\partial \rho u}{\partial x} + \frac{\partial \rho v}{\partial y} + \frac{\partial \rho w}{\partial z} = 0\,, \tag{2.1}$$

but the momentum conservation equations simplify to

$$\rho\left(u\frac{\partial u}{\partial x} + v\frac{\partial u}{\partial y} + w\frac{\partial u}{\partial z}\right) \approx -\frac{\partial p}{\partial x} + \frac{\partial}{\partial y}\left[\mu\frac{\partial u}{\partial y}\right]\,,$$

$$\frac{\partial p}{\partial y} \approx 0 \tag{2.2}$$

and

$$\rho\left(u\frac{\partial w}{\partial x} + v\frac{\partial w}{\partial y} + w\frac{\partial w}{\partial z}\right) \approx -\frac{\partial p}{\partial z} + \frac{\partial}{\partial y}\left[\mu\frac{\partial u}{\partial y}\right]\,.$$

For a turbulent flow, Reynolds averaging is usually employed to obtain equations for the meanflow quantities. Variables are decomposed into meanflow and fluctuating components such that $\rho = \bar{\rho} + \rho'$, $u = \bar{u} + u'$, $v = \bar{v} + v'$, $w = \bar{w} + w'$ and $\mu = \bar{\mu} + \mu'$. These expressions are substituted in Equations 2.1 and 2.2 which are then ensemble averaged.

The averaging procedure results in the mass conservation equation taking the form

$$\frac{\partial \bar{\rho}\bar{u}}{\partial x} + \frac{\partial \overline{\rho v}}{\partial y} + \frac{\partial \bar{\rho}\bar{w}}{\partial z} + \frac{\partial \overline{\rho' u'}}{\partial x} + \frac{\partial \overline{\rho' w'}}{\partial x} = 0 \, . \tag{2.3}$$

Now, in a boundary-layer, $\overline{\rho' u'} \ll \bar{\rho}\bar{u}$ and $\overline{\rho' w'} \ll \bar{\rho}\bar{w}$ so that the last two terms in Equation 2.3 can be ignored. These terms also appear in the ensemble-averaged momentum equations, which are not presented here, but there are also ignored. This is generally a good assumption except in the region of separation due to vanishing skin friction [1, 21]. However, $\overline{\rho' v'} \approx \bar{\rho}\bar{v}$ and is hence retained, embedded in the second term of Equation 2.3.

The transverse momentum equation,

$$\frac{\partial p}{\partial y} \approx -\frac{\partial}{\partial y}\left(\bar{\rho}\overline{v' v'}\right) \, ,$$

is no longer trivial but the Reynolds normal stress, $\bar{\rho}\overline{v' v'}$, is usually also neglected. This term is important, however, in supersonic turbulent flow with adverse pressure gradients [21, pages 606, 626].

In compressible flow, mass-weighted variables are traditionally employed in the Reynolds averaging to decouple density from the other variables (see for example [1, page 217]). For the present development, this is only performed with the transverse velocity. The mass-weighted velocity $\tilde{v}$ is defined such that

$$\tilde{v} = \left(\bar{\rho}\bar{v} + \overline{\rho' v'}\right) / \bar{\rho}$$

and, therefore, $\overline{\rho v} = \bar{\rho}\tilde{v}$.

Henceforth, the pressure p will be set equal to the value at the edge of the boundary layer p_e. In addition, the notation will be modified slightly for the sake of brevity in that the overbar will be abandoned. By virtue of Bernoulli's theorem applied to the external flow region, pressure gradient terms in the momentum equations can be written in terms of velocity gradients,

$$\frac{\partial p_e}{\partial x} = -\rho_e \left(u_e \frac{\partial u_e}{\partial x} + w_e \frac{\partial w_e}{\partial x} \right)$$

and

$$\frac{\partial p_e}{\partial z} = -\rho_e \left(u_e \frac{\partial u_e}{\partial z} + w_e \frac{\partial w_e}{\partial z} \right) .$$

If, furthermore, the external flow is assumed to be irrotational, $\vec{\nabla} \times \vec{q}_e = 0$, then

$$\frac{\partial p_e}{\partial x} = -\rho_e \left(u_e \frac{\partial u_e}{\partial x} + w_e \frac{\partial u_e}{\partial z} \right)$$

and

$$\frac{\partial p_e}{\partial z} = -\rho_e \left(u_e \frac{\partial w_e}{\partial x} + w_e \frac{\partial w_e}{\partial z} \right) .$$

Finally, introducing the equality sign, the differential form of the relations needed in § 2.2 are obtained,

$$\frac{\partial \rho u}{\partial x} + \frac{\partial \rho \tilde{v}}{\partial y} + \frac{\partial \rho w}{\partial z} = 0 ,$$

$$\rho \left(u \frac{\partial u}{\partial x} + \tilde{v} \frac{\partial u}{\partial y} + w \frac{\partial u}{\partial z} \right) = \rho_e \left(u_e \frac{\partial u_e}{\partial x} + w_e \frac{\partial u_e}{\partial z} \right) + \frac{\partial \tau_x}{\partial y} \tag{2.4}$$

and

$$\rho \left(u \frac{\partial w}{\partial x} + \tilde{v} \frac{\partial w}{\partial y} + w \frac{\partial w}{\partial z} \right) = \rho_e \left(u_e \frac{\partial w_e}{\partial x} + w_e \frac{\partial w_e}{\partial z} \right) + \frac{\partial \tau_z}{\partial y} ,$$

where the overall stresses

$$\tau_x = \mu \frac{\partial u}{\partial y} - \rho \overline{u'v'}$$

and

$$\tau_z = \mu \frac{\partial w}{\partial y} - \rho \overline{w'v'}$$

include the Reynolds stress terms.

The various assumptions inherent in these equations limit their range of applicability. In particular, in the neighborhood of separated flow, both due to vanishing skin friction and the three-dimensional focusing of characteristic lines, many of the physical assumptions made so far are strictly not valid [3].

2.2 Integral Form

Integral equations are derived by integrating combinations of Equations 2.4 in the y direction in such a manner that they can be written as a function of many kinds of of physically-meaningful quantities, depending on the desired closure [21, p. 513]. In the literature, momentum-integral relations are ubiquitously found with one or more additional relations, usually for entrainment, but also for kinetic energy, turbulent energy, various moments of momentum and others.

The calculation presented in this thesis makes use of the momentum-integral relations with an additional equation for the kinetic energy. The entrainment relation was not considered because closure would entail use of the boundary layer thickness δ, which historically has produced results inferior to the momentum-integral relation [21, p. 516] due, presumably, to the amorphous nature of δ in experimental work.

The derivation of the equations is shown in some detail.

2.2.1 Momentum Relations

The momentum-integral equation along x can be derived by considering the combination $(u - u_e) \times$ continuity-equation + x-momentum-equation, which can be compactly written as

$$\frac{\partial}{\partial x}\left[\rho u\left(u-u_e\right)\right]+\frac{\partial}{\partial y}\left[\rho \tilde{v}\left(u-u_e\right)\right]+\frac{\partial}{\partial z}\left[\rho w\left(u-u_e\right)\right]+$$
$$\left(\rho_e u_e-\rho u\right)\frac{\partial u_e}{\partial x}+\left(\rho_e w_e-\rho w\right)\frac{\partial u_e}{\partial z}=\frac{\partial \tau_x}{\partial y}.$$

This equation is integrated with respect to y, from the wall, where $y = 0$, to the edge of the boundary layer, where $y = \delta$, to yield

$$\frac{\partial}{\partial x}\left(\rho_e q_e^2 \theta_{xx}\right)+\frac{\partial}{\partial z}\left(\rho_e q_e^2 \theta_{xz}\right)+\rho_e q_e \delta_x^* \frac{\partial u_e}{\partial x}+\rho_e q_e \delta_z^* \frac{\partial u_e}{\partial z}=\tau_{x_w}, \tag{2.5}$$

where the displacement thicknesses, δ_x^* and δ_z^*, are defined as

$$\rho_e q_e \delta_x^* = \int_0^\delta \left(\rho_e u_e - \rho u\right) dy$$

and

$$\rho_e q_e \delta_z^* = \int_0^\delta \left(\rho_e w_e - \rho w\right) dy,$$

and the momentum thicknesses, θ_{xx} and θ_{zz}, are defined as

$$\rho_e q_e^2 \theta_{xx} = \int_0^\delta (u_e - u)\rho u \, dy$$

and

$$\rho_e q_e^2 \theta_{xz} = \int_0^\delta (u_e - u)\rho w \, dy.$$

The partial-differentiation and integration in Equation 2.5 are interchangeable because, in compliance with Leibnitz's rule, the integrands are zero between $y = \delta$ and $y = \infty$. Furthermore, the second term disappears because $\tilde{v} = 0$ at the lower limit and $(u - u_e) = 0$ at the upper limit.

An equation for the momentum in the z direction can similarly be obtained by considering the combination $(w - w_e) \times$ continuity-equation + z-momentum-equation, which can be expressed as

$$\frac{\partial}{\partial x}[\rho u(w - w_e)] + \frac{\partial}{\partial y}[\rho \tilde{v}(w - w_e)] + \frac{\partial}{\partial z}[\rho w(w - w_e)] + \\ (\rho_e u_e - \rho u)\frac{\partial w_e}{\partial x} + (\rho_e w_e - \rho w)\frac{\partial w_e}{\partial z} = \frac{\partial \tau_z}{\partial y}\,.$$

As before, this equation is integrated along y to yield

$$\frac{\partial}{\partial x}(\rho_e q_e^2 \theta_{zx}) + \frac{\partial}{\partial z}(\rho_e q_e^2 \theta_{zz}) + \rho_e q_e \delta_x^* \frac{\partial w_e}{\partial x} + \rho_e q_e \delta_z^* \frac{\partial w_e}{\partial z} = \tau_{z_w}\,,$$

where the momentum thicknesses, θ_{zx} and θ_{xz}, are defined as

$$\rho_e q_e^2 \theta_{zx} = \int_0^\delta (w_e - w)\rho u\, dy$$

and

$$\rho_e q_e^2 \theta_{zz} = \int_0^\delta (w_e - w)\rho w\, dy\,.$$

These momentum integral relations are simply three-dimensional extensions of the well-known von Kármán equation in two dimensions.

2.2.2 Kinetic-Energy Relation

The relation involving the kinetic-energy thicknesses is also readily derived. The expression $(q^2 - q_e^2) \times$ continuity-equation + $2u \times$ x-momentum-equation + $2w \times$ z-momentum-equation can be written as

$$
\begin{aligned}
&\frac{\partial}{\partial x}[\rho u(q^2 - q_e^2)] + \frac{\partial}{\partial x}[\rho\tilde{v}(q^2 - q_e^2)] + \frac{\partial}{\partial x}[\rho w(q^2 - q_e^2)] \\
&\qquad - (\rho_e - \rho)u\frac{\partial q_e^2}{\partial x} - (\rho_e - \rho)w\frac{\partial q_e^2}{\partial z} = 2u\frac{\partial \tau_x}{\partial y} + 2w\frac{\partial \tau_z}{\partial y} \,.
\end{aligned}
$$

Integration along y yields

$$
\frac{\partial}{\partial x}(\rho_e q_e^3 \theta_x^*) + \frac{\partial}{\partial z}(\rho_e q_e^3 \theta_z^*) + \rho_e q_e \delta_x^{**}\frac{\partial q_e^2}{\partial x} + \rho_e q_e \delta_z^{**}\frac{\partial q_e^2}{\partial z} = 2D \,.
$$

where

$$
\rho_e q_e^3 \theta_x^* = \int_0^\delta (q_e^2 - q^2)\rho u \, dy \,,
$$

$$
\rho_e q_e^3 \theta_z^* = \int_0^\delta (q_e^2 - q^2)\rho w \, dy \,,
$$

$$
\rho_e q_e \delta_x^{**} = \int_0^\delta (\rho_e - \rho) u \, dy \,,
$$

$$
\rho_e q_e \delta_z^{**} = \int_0^\delta (\rho_e - \rho) w \, dy
$$

and

$$
D = \int_0^\delta \left(\tau_x \frac{\partial u}{\partial y} + \tau_z \frac{\partial w}{\partial y} \right) dy \,.
$$

D is known as the dissipation or shear-work integral and can be written as the sum of two components, one due to the wall-normal gradient of velocity in the x direction and the other due to the gradient in the z direction, so that

$$
D = D_x + D_z \,.
$$

2.2.3 Summary

For clarity of presentation, the equations that form the basis of the calculation method are reproduced below.

$$\begin{aligned}
&\frac{\partial}{\partial x}\left(\rho_e q_e^2 \theta_{xx}\right) + \frac{\partial}{\partial z}\left(\rho_e q_e^2 \theta_{xz}\right) + \rho_e q_e \delta_x^* \frac{\partial u_e}{\partial x} + \rho_e q_e \delta_z^* \frac{\partial u_e}{\partial z} = \tau_{x_w} \\
&\frac{\partial}{\partial x}(\rho_e q_e^2 \theta_{zx}) + \frac{\partial}{\partial z}(\rho_e q_e^2 \theta_{zz}) + \rho_e q_e \delta_x^* \frac{\partial w_e}{\partial x} + \rho_e q_e \delta_z^* \frac{\partial w_e}{\partial z} = \tau_{z_w} \qquad (2.6) \\
&\frac{\partial}{\partial x}(\rho_e q_e^3 \theta_x^*) + \frac{\partial}{\partial z}(\rho_e q_e^3 \theta_z^*) + \rho_e q_e \delta_x^{**} \frac{\partial q_e^2}{\partial x} + \rho_e q_e \delta_z^{**} \frac{\partial q_e^2}{\partial z} = 2D
\end{aligned}$$

2.3 Primary Variables

Equations 2.6 are functions of many variables. In the next chapter, all of these variables will be related to three primary ones through empirical relations. The primary variables are chosen to be θ_{xx}, δ_x^* and $\tan(\beta_w)$, where the coordinate x is parallel to the external-flow streamline. Figure 2.1 shows a typical distribution of velocity in a three-dimensional boundary layer along the normal to the wall. The variable β_w is the angular difference between the direction of the external-flow streamline and that of the limiting wall streamline. The limiting wall streamline, or simply limiting streamline, is the streamline in the limit of vanishing distance from the wall.

It will be useful, at this juncture, to define an independent coordinate system in terms of external-flow streamlines. One family of a set of mutually orthogonal coordinate curves is formed by the projection onto the surface of the streamlines just external to the boundary layer. The direction of an external streamline is called the streamwise direction and boundary-layer flow normal to an external streamline and parallel to the surface is called crossflow. The boundary layer in Figure 2.1 is shown in this coordinate system.

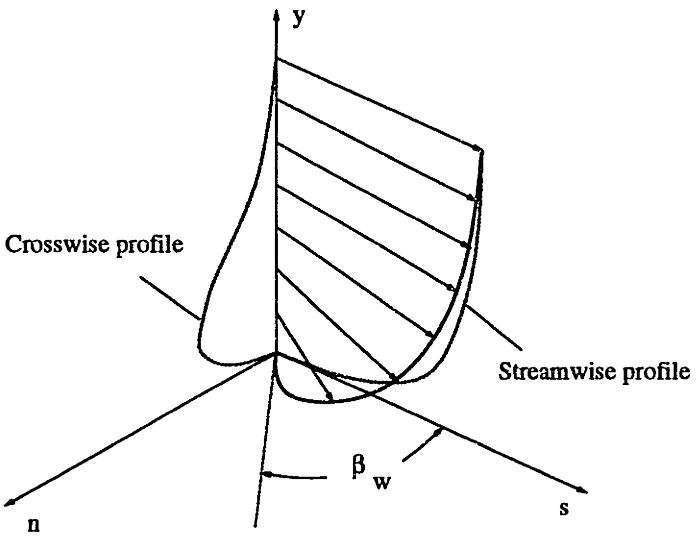

Figure 2.1: Velocity distribution in a typical 3D boundary layer

The two orientation-dependent primary variables when in this coordinate system will be written with numeric subscripts: θ_{11} and δ_1^*. As a general syntactic rule, in this coordinate system, x and z will be replaced by 1 and 2 respectively, in variable subscripts.

For notational efficiency, the vector of primary unknowns,

$$\boldsymbol{U} = \begin{bmatrix} \theta_{11} \\ \beta_w \\ \delta_1^* \end{bmatrix},$$

is defined.

2.4 Nature of the System

2.4.1 Domains of Influence and Dependence

The hyperbolic nature of the system of integral equations is exceedingly important in their calculation. The characteristic directions determine whether or not the solution of the equations can be marched in a particular direction.

Consider, first, the differential form of the equations. The study of the characteristics of a system involves only the highest derivative terms in each equation. The characteristic determinant yields a characteristic equation; the sign of the roots of this equation describes the nature of the system. The characteristic equation for the incompressible Navier-Stokes system has no real root, expressing their well-known elliptic properties. On the other hand, in the case of the boundary-layer Equations 2.1 and 2.2, all the roots are real and equal, indicating their parabolic nature [19].

A physical interpretation was offered by Raetz who studied the laminar boundary-layer equations [10, 12]. In the boundary layer approximation, the equations are hyperbolic in surfaces parallel to the wall and, therefore, imply the existence of domains of dependence and influence in the same way as in any other hyperbolic system. Information is convected along streamlines in the boundary layer and also transported along lines normal to the wall by viscous diffusion. On this basis, Raetz articulated an "influence principle" which stated that conditions at some point in the boundary layer depend only on conditions in a wedge-like domain of dependence, extending upstream from the point, bounded by two surfaces normal to the wall which just enclose all the streamlines passing through their line of intersection. The downstream extension defines the domain of influence.

The idea of subcharacteristics, which are defined as the characteristics of the corresponding inviscid equations, can be used to arrive at the same physical picture as that of Raetz [19]. For both the Navier-Stokes system and the boundary layer system, subcharacteristics are associated with streamlines. In the case of the Navier-Stokes

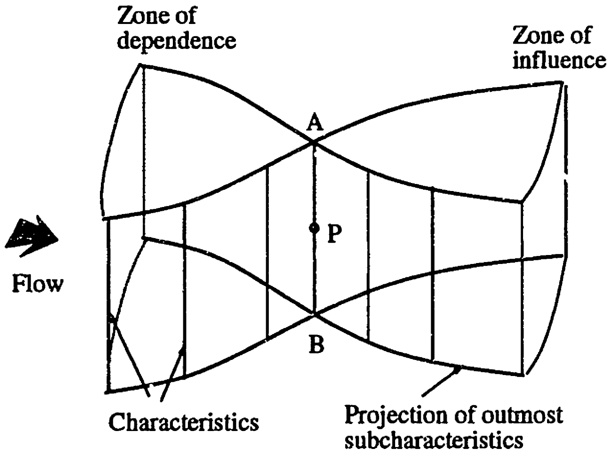

Figure 2.2: Zones of influence and dependence in a 3D boundary layer

equations, the convection of a disturbance along the streamlines is masked by diffusion; in the case of the boundary-layer equations, on the other hand, diffusion prevails only in the direction normal to the surface and, therefore, subcharacteristics or streamlines do play a role in determining the main flow structure. Consequently, a disturbance at the point P in Figure 2.4.1 first affects instantly — in the incompressible limit — the normal line AB through P, and is then convected downstream by all the streamlines crossing AB.

In the case of laminar flow, the angle included between the surfaces bounding the domains of dependence and influence can never be smaller than the wall crossflow angle; the two are usually equal. One of the bounding surfaces is tangential to the external streamlines and the other is tangential to the limiting streamline [10]. In the case of turbulent flow, however, Wesseling suggested that the extent of the domains of dependence and influence may be smaller on the basis of a set of equations which are hyperbolic in planes normal to the wall as well in the surfaces parallel to it [10, 20].

Consider, now, the integral form of the equations. For an incompressible, turbulent system of momentum-integral and entrainment relations, Cousteix and Houdeville show that the roots of the characteristic equation are real and distinct, indicating that the system is hyperbolic [4]. A qualitatively similar result was also obtained in a separate study by Myring who employed slightly different closure relationships [9]. Systems of integral equations are expected to be hyperbolic because the elliptic/diffusive nature of the differential equations in the direction normal to the wall is integrated out.

The number of roots of the characteristic equation (these roots are referred to as characteristic lines or directions on the basis of their physical interpretation) depends on the number of global equations employed. Therefore, for the set of integral equations in this thesis, there are three equations. Additional equations can be employed but the main features of the flow are adequately described by three [4].

One of the characteristic lines can be identified with the limiting wall streamline [4]. The other two lie between the external-flow streamline and the limiting wall streamline [3].

The hyperbolicity of the set of integral equations implies the relevance of the concept of domains of dependence and influence. This has practical consequences for their calculation. For example, the number of boundary conditions needed is the same as the number of characteristics entering the domain. In general, the development of a numerical scheme must incorporate knowledge of characteristic directions.

2.4.2 Calculation of Characteristic Directions

Equations 2.6 can be written in a form where the left hand side includes all the derivatives of the vector of primary unknowns $\boldsymbol{U}$,

$$\frac{\partial\theta_{11}}{\partial s} + \frac{\partial\theta_{12}}{\partial n} = A_1\,,$$

$$\frac{\partial\theta_{21}}{\partial s} + \frac{\partial\theta_{22}}{\partial n} = A_2$$

and

$$\frac{\partial \theta_1^*}{\partial s} + \frac{\partial \theta_2^*}{\partial n} = A_3 .$$

Note that the derivatives are taken with respect to the streamwise and crossflow directions. This system of equations is further manipulated so that the primary unknowns appear explicitly,

$$\begin{bmatrix} 1 & 0 & 0 \\ \frac{\partial \theta_{21}}{\partial \theta_{11}} & \frac{\partial \theta_{21}}{\partial \tan(\beta_w)} & \frac{\partial \theta_{21}}{\partial \delta_1^*} \\ \frac{\partial \theta_1^*}{\partial \theta_{11}} & \frac{\partial \theta_1^*}{\partial \tan(\beta_w)} & \frac{\partial \theta_1^*}{\partial \delta_1^*} \end{bmatrix} \frac{\partial \boldsymbol{U}}{\partial s} + \begin{bmatrix} \frac{\partial \theta_{12}}{\partial \theta_{11}} & \frac{\partial \theta_{12}}{\partial \tan(\beta_w)} & \frac{\partial \theta_{12}}{\partial \delta_1^*} \\ \frac{\partial \theta_{22}}{\partial \theta_{11}} & \frac{\partial \theta_{22}}{\partial \tan(\beta_w)} & \frac{\partial \theta_{22}}{\partial \delta_1^*} \\ \frac{\partial \theta_2^*}{\partial \theta_{11}} & \frac{\partial \theta_2^*}{\partial \tan(\beta_w)} & \frac{\partial \theta_2^*}{\partial \delta_1^*} \end{bmatrix} \frac{\partial \boldsymbol{U}}{\partial n} = \boldsymbol{A}' ,$$

and then,

$$\frac{\partial \boldsymbol{U}}{\partial s} + B \frac{\partial \boldsymbol{U}}{\partial n} = \boldsymbol{A}'' ,$$

where

$$B = \begin{bmatrix} 1 & 0 & 0 \\ \frac{\partial \theta_{21}}{\partial \theta_{11}} & \frac{\partial \theta_{21}}{\partial \tan(\beta_w)} & \frac{\partial \theta_{21}}{\partial \delta_1^*} \\ \frac{\partial \theta_1^*}{\partial \theta_{11}} & \frac{\partial \theta_1^*}{\partial \tan(\beta_w)} & \frac{\partial \theta_1^*}{\partial \delta_1^*} \end{bmatrix}^{-1} \begin{bmatrix} \frac{\partial \theta_{12}}{\partial \theta_{11}} & \frac{\partial \theta_{12}}{\partial \tan(\beta_w)} & \frac{\partial \theta_{12}}{\partial \delta_1^*} \\ \frac{\partial \theta_{22}}{\partial \theta_{11}} & \frac{\partial \theta_{22}}{\partial \tan(\beta_w)} & \frac{\partial \theta_{22}}{\partial \delta_1^*} \\ \frac{\partial \theta_2^*}{\partial \theta_{11}} & \frac{\partial \theta_2^*}{\partial \tan(\beta_w)} & \frac{\partial \theta_2^*}{\partial \delta_1^*} \end{bmatrix} .$$

The system is diagonalized through multiplication by the inverse of the matrix of eigenvectors of B,

$$T^{-1} \frac{\partial \boldsymbol{U}}{\partial s} + T^{-1} \boldsymbol{B} T T^{-1} \frac{\partial \boldsymbol{U}}{\partial n} = T^{-1} \boldsymbol{A}'' .$$

Then, rewriting in terms of the vector of characteristic variables $\boldsymbol{W} = T^{-1} \boldsymbol{U}$,

$$\frac{\partial \boldsymbol{W}}{\partial s} + \Lambda \frac{\partial \boldsymbol{W}}{\partial n} = \boldsymbol{A}''' ,$$

the individual equations decouple. Here, Λ is the diagonal matrix of eigenvalues. These eigenvalues are also the roots of the characteristic equation of B and represent the tangent of the angle that the characteristic lines make with the external streamline.

Empirical relationships, to be introduced in the following chapter, enter the analysis through these Jacobian matrix elements. Calculation of reasonable characteristic directions, therefore, constitutes a demonstration of the coherence of the employed closure.

Chapter 3

Empirical Relationships for Closure

3.1 Introduction

Equations 2.6 form the basis of the calculation method, but to make the problem determinate, the number of unknowns contained therein must be reduced to three. This is done by relating all variables to the three primary unknowns, θ_{11}, δ_1^* and $\tan(\beta_w)$ using assumed forms of velocity profiles together with empirical skin-friction and dissipation relations derived from experiment. The dissipation formula requires the assumption of a turbulence model.

The traditional methodology in three-dimensional closure has been to assume two-dimensional-like behavior of the boundary layer in the streamwise direction. One fortunate outcome of this assumption is that empirical correlations of the streamwise variables in three-dimensional flows can draw a considerable amount of information from the better-explored two-dimensional flows. Fortunately, there is a close experimental resemblance between three-dimensional streamwise profiles and two-dimensional boundary layers [10]. Such an approach is obviously most valid when the crossflow is small.

In the crossflow direction, a suitable model for the velocity profile is formulated in terms of the streamwise profile and is used to relate the crossflow variables to the streamwise ones.

In this thesis, since the accuracy of closure is not the major issue, only equilibrium models of the flow are considered. More sophisticated closure which takes into account turbulent lag effects important in three-dimensional flow (for example the shear-stress vector lagging behind the velocity-gradient vector) have been widely used [18]. However, the extra effort entailed was not deemed necessary for this method.

It will be useful to define a set of shape factors that appear in the expressions in the following two sections. These shape factors are simply ratios of the considered variable to θ_{11} so that

$$H = \delta_1^*/\theta_{11}, \quad H_{E_{11}} = E_{11}/\theta_{11}, \quad H_{\delta_1^{**}} = \delta_1^{**}/\theta_{11} \text{ and } H_{\theta_\rho} = \theta_\rho/\theta_{11}\,.$$

In the following sections, the overbar notation will be employed to denote corresponding incompressible values (where density is assumed constant through the boundary layer) of compressible variables.

3.2 Streamwise Closure

3.2.1 Streamwise Velocity Profile

Turbulent boundary layers have a two-layer structure where the thickness of each layer scales differently with $\overline{Re_\theta}$. Therefore, at least two independent parameters are needed to adequately describe a velocity profile.

The analytical formula that is employed in this calculation method was developed by Swafford [15]. It is the sum of two independent transcendental functions, one expressed in terms of the inner variable $\bar{y}^+$ and the other expressed in terms of the outer variable $y/\bar{\theta}$,

$$\bar{u}^+ = \frac{s}{0.09}\arctan\left(0.09\bar{y}^+\right) + \left(\bar{u}_e^+ - \frac{s\pi}{0.18}\right)\tanh^{1/2}\left[a\left(\frac{y}{\bar{\theta}}\right)^b\right]\,.$$

Here $\bar{y}^+ = \overline{Re_\theta}$, $s = \bar{c}_f/|\bar{c}_f|$ and

$$\frac{u}{u_e} = \frac{\bar{u}^+}{\bar{u}_e^+}\,,$$

where $\bar{u}_e^+ = (2/|\bar{c}_f|)^{1/2}$. The factor s appears because this expression is valid for separated as well as attached flows. The two parameters that describe the given boundary-layer profile are a and b and these are functions of $\bar{c}_f$, $\bar{H}$ and $\overline{Re_\theta}$.

The compressible and corresponding incompressible values of θ are related by

$$\frac{\theta}{\bar{\theta}} = 1 - \frac{0.92\,M_e^2}{7.09 + M_e^2} \tanh[1.49(\bar{H} - 0.9)]\,,$$

a formula developed by Whitfield [23].

3.2.2 Skin Friction

Following the observation that the velocity distribution in the streamwise direction may be represented by profile families developed for two-dimensional flows, it has often been assumed that the streamwise component of skin friction may also be obtained by using skin-friction relations applicable to two-dimensional flows [10]. The presence of the law-of-the-wall as one component of the two-parameter family of profiles described above enables one to correlate $\bar{u}_e^+$ in terms of two integral parameters, for example H and $Re_{\theta_{11}}$, thereby yielding an expression for the streamwise component of skin friction. The relation employed in this calculation method,

$$\bar{c}_f = \frac{0.3e^{-1.33\bar{H}}}{\left(\log_{10} \overline{Re_\theta}\right)^{1.74+0.31\bar{H}}} + \left(1.1 \times 10^{-4}\right) \left[\tanh\left(4 - \frac{\bar{H}}{0.875}\right) - 1\right]\,,$$

was developed by Swafford [15]. The compressible value is given by

$$\frac{c_{f_1}}{\bar{c}_f} = \frac{1}{F_c}\,,$$

where

$$F_c = \sqrt{1 + \frac{\gamma - 1}{2} M_e^2}$$

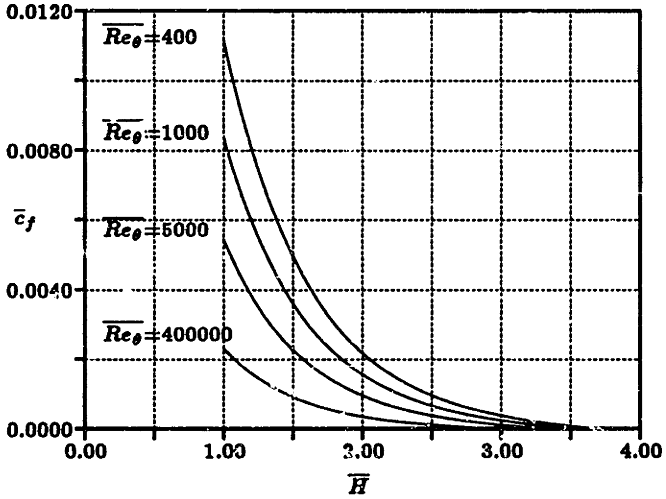

Figure 3.1: Empirical variation of streamwise skin friction for $M_e = 0$

for a gas with constant specific heat ratio γ, and a constant total enthalpy at the boundary-layer edge. A representative family of curves is shown in Figure 3.1. As expected for turbulent flow, the variation is very sensitive at low Re_θ but asymptotes rapidly at higher Re_θ. The two-dimensional separation value for $\overline{H}$ also exhibits the same behavior as a function of Re_θ.

The streamwise value of the shear stress, required by Equations 2.6, is related to the skin friction through its definition,

$$\tau_{1_w} \equiv \left(\frac{1}{2}\rho_e q_e^2\right) c_{f_1} .$$

The assumption that the streamwise component of wall shear is related to the streamwise velocity profile implies that the law of the wall applies to the velocity profile in its usual two dimensional form. Strictly, this is incorrect. This assumption is likely to be of more consequence, however, in methods employing differential equations while in the integral methods, errors thus introduced are unlikely to be more serious than those originating from other sources [10].

3.2.3 Kinetic-Energy Thickness

A thickness E_{11} that depends only on the streamwise velocity in the boundary layer is defined such that

$$\rho_e q_e^3 E_{11} = \int_0^\delta \rho u (u_e^2 - u^2)\, dy .$$

This thickness is the streamwise component of θ_1^* and can be correlated to H and $Re_{\theta_{11}}$ through the streamwise velocity profile. The correlation employed is one due to Drela [6],

$$\overline{H_{E_{11}}} = \begin{cases} 1.505 + \frac{4}{\overline{Re_\theta}} + \left(0.165 - \frac{1.6}{\sqrt{\overline{Re_\theta}}}\right) \frac{(H_o - \bar{H})^{1.6}}{\bar{H}} & \text{if } \bar{H} \le H_o \\ 1.505 + \frac{4}{\overline{Re_\theta}} + (\bar{H} - H_o)^2 \left(\frac{0.04}{\bar{H}} + 0.007 \frac{\ln(\overline{Re_\theta})}{\left(\bar{H} - H_o + \frac{4}{\ln(\overline{Re_\theta})}\right)^2} \right) & \text{if } \bar{H} > H_o , \end{cases}$$

where

$$H_o = 3.0 + \frac{400}{\overline{Re_\theta}} .$$

The corresponding compressible quantity is obtained from the relation

$$H_{E_{11}} = \frac{\overline{H_{E_{11}}} + 0.028\, M_e^2}{1 + 0.014\, M_e^2} ,$$

due to Whitfield et. al. [22].

In addition to this relation, another proposed by Whitfield et. al. [23] was considered. It produced reasonable results almost indistinguishable from those using Drela's equation. However, for one calculation (the van den Berg/Elsenaar infinite wing in Chapter 5) it failed to yield characteristic directions coherent with the computed result. The failure was presumably due to an assumption in their derivation, as Drela notes, that effectively eliminated the dependence on Reynolds number [6]. Consequently, the sensitivity of the characteristic directions to the Jacobian-matrix elements involving

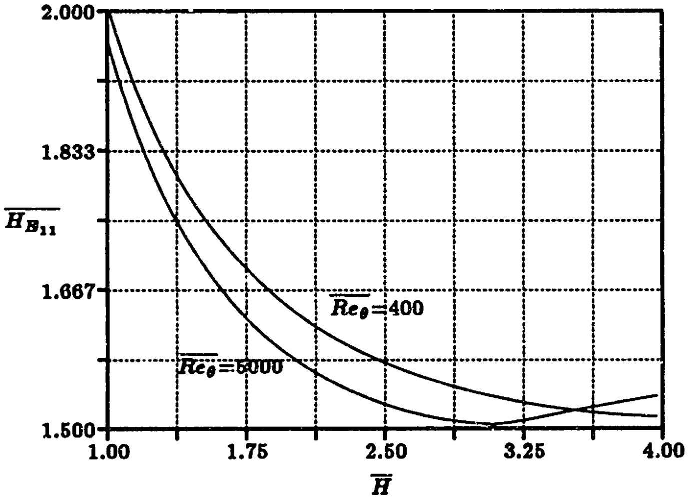

Figure 3.2: Empirical variation of streamwise kinetic energy for $M_e = 0$

$H_{E_{11}}$, especially at low Reynolds numbers, would likely have yielded highly-erroneous results. Drela's expression does not include this simplification. The variation of $\overline{H_{E_{11}}}$ with $\overline{H}$ is shown for two values of $\overline{Re_\theta}$ in Figure 3.2 .

3.2.4 Density Thickness

The correlation for compressible density thickness employed is only a function of the shape parameter and Mach number,

$$H_{\delta_1^{**}} = \left[\frac{0.064}{\bar{H} - 0.8} + 0.251\right] M_e^2 \,,$$

and is given by Whitfield et. al. [23]. It is also necessary to define an auxiliary density thickness,

$$\rho_e \theta_\rho = \int_0^\delta (\rho_e - \rho)\, dy \,,$$

which is not to be confused with δ_1^{**} or δ_2^{**}. Donegan [16] correlated H_{θ_ρ} with $\bar{H}$ and M_e,

$$H_{\theta_\rho} = M_e^2 \, (0.185 \, \bar{H} + 0.150) \, .$$

It is required in some definitions of crossflow variables in a later section.

3.2.5 Dissipation

The coefficient of dissipation due to the surface-normal gradient of velocity in the streamwise direction was derived by numerically evaluating the dissipation integral using a constant laminar plus turbulent shear stress in the region very near the wall, an eddy-viscosity model in the inner and outer regions and the streamwise velocity profile of Whitfield et. al. [16, 22],

$$c_{D_1} = \frac{0.009 - 0.011 e^{-0.15 \bar{H}^{2.1}} + 3.0 \times 10^{-5} e^{0.117 \bar{H}^2} + a(\overline{Re_\theta})^{-0.574}}{F_c \, (1 + 0.05 \, M_e^{1.4})} \, ,$$

where $c_{D_1} = D_1 / \rho_e q_e^3$ and

$$a = \begin{cases} 0.438 - 0.280 \, \bar{H} & \text{if } \bar{H} \leq 3.5 \\ 0.160(\bar{H} - 3.5) - 0.550 & \text{if } \bar{H} > 3.5 \, . \end{cases}$$

This expression is also taken from Whitfield et. al. [23]. A representative family of curves is shown in Figure 3.3. The variation is quite severe at low values of Re_θ.

3.3 Crosswise Closure

3.3.1 Crosswise Velocity Profile

There are two widely used crossflow models. The earlier was proposed by Mager (1952) and is parabolic in the hodograph plane [8]. The other was suggested by Johnston (1957) and is hodographically triangular [7]. Both of these models are unidirectional so that the crossflow velocity does not change sign along the normal to the surface.

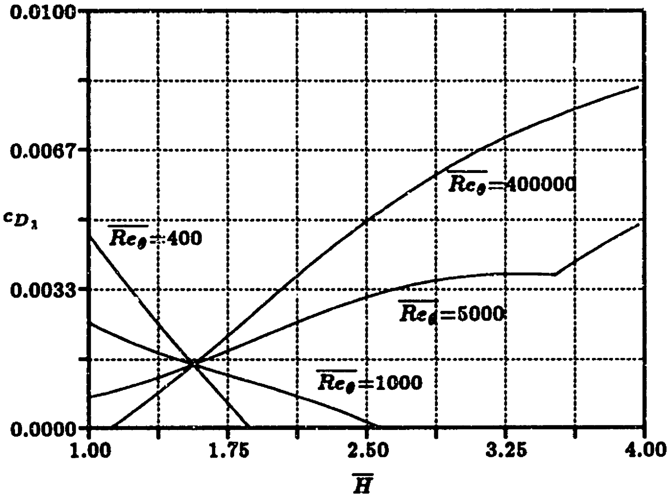

Figure 3.3: Empirical variation of streamwise dissipation for $M_e = 0$

The Johnston model, however, contains two parameters, one more than Mager's, and is hence a considerable improvement over many of the earlier models. More sophisticated models that allow bidirectional skewing, for example that of Smith (1966) [13], have also been proposed but have produced worse correlations with experiment as compared to the Mager or Johnston models [21, pg. 544] in spite of the intrinsic restriction in the uni-directional models of the limiting-streamlines being normal to the surface isobar [13, 21].

The crossflow model employed in this calculation method is Johnston's triangular model which defines two distinct layers. In the thin layer adjacent to the surface, the crosswise velocity is related to the streamwise one by

$$\frac{w}{u} = \tan(\beta_w) \; .$$

Over the remaining portion of the boundary layer,

$$\frac{w}{q} = A\left[1 - \left(\frac{u}{q}\right)\right] \; .$$

The parameter A is a measure of the crossflow magnitude and can be related to β_w. Smith provides such a relation,

$$A = -\tan(\beta_w)\left[\frac{\sqrt{c_{f_1}\cos(\beta_w)(1+0.18\,M_e^2)}}{0.10-\sqrt{c_{f_1}\cos(\beta_w)(1+0.18\,M_e^2)}}-1\right],$$

which includes the effects of compressibility [14].

While A appears explicitly instead of β_w in the remaining relations, the latter is, nevertheless, chosen as a primary variable because it is uniquely related A. The reverse is not true.

3.3.2 Skin-friction

Following Smith [13, 14] and Myring [9], the crossflow component of skin friction is easily related to the streamwise one through the limiting-streamline angle,

$$c_{f_2} = -\tan(\beta_w)\,c_{f_1}\,.$$

The minus sign appears due to the convention of considering counter-clockwise angles positive. The crosswise shear stress, as required in Equations 2.6, is identically related to the skin-friction,

$$\tau_{2_w} \equiv \left(\frac{1}{2}\rho_e q_e^2\right) c_{f_2}\,.$$

3.3.3 Dissipation

The dissipation due to the crossflow is expressed in terms of that due to the streamwise flow and the parameter A,

$$c_{D_2} = \left(\frac{|A|}{14667\,c_{D_1}+3.0}\right)^{\frac{|A|+10.0}{1020\,c_{D_1}+4.0}},$$

where $c_{D_1} = D_1/\rho_e q_e^3$. This correlation was derived by numerically evaluating the integral

$$\int_0^\delta |\tan(\beta)|\tau_1 \frac{\partial u}{\partial y}\, dy\,,$$

using Cebeci-Smith's two-layer eddy-viscosity model [2] and the streamwise velocity profile discussed in § 3.2.1.

3.3.4 Crossflow Thicknesses

The remaining thickness variables can be readily related to the streamwise ones through the shape factors using the assumed shape of the crossflow velocity profile. These are listed below.

$$\begin{aligned}
\theta_{21} &= -A\,\theta_{11} \\
\delta_2^* &= \theta_{21}(H - H_{\theta_\rho}) \\
\theta_{22} &= -A\,\theta_{12} \\
\delta_2^{**} &= A\,(\theta_\rho - \delta_1^{**}) \\
E_{12} &= \theta_{12} + \theta_{21}(H_{E_{11}} - 2) \\
E_{21} &= -\theta_{22} - A\,E_{12} \\
E_{22} &= -A\,(E_{21} - \theta_{22})
\end{aligned}$$

The kinetic-energy thicknesses are defined to be

$$\rho_e q_e^3 E_{12} = \int_0^\delta \rho w (u_e^2 - u^2)\, dy\,,$$

$$\rho_e q_e^3 E_{21} = -\int_0^\delta \rho u w^2\, dy$$

and

$$\rho_e q_e^3 E_{22} = -\int_0^\delta \rho u^3\, dy\,.$$

These thicknesses are simply components of the previously-defined thicknesses θ_1^* and θ_2^*,

$$\theta_1^* = E_{11} + E_{21}$$

and

$$\theta_2^* = E_{12} + E_{22} .$$

In addition, there is the identity

$$\theta_{12} \equiv \theta_{21} - \delta_2^* .$$

It is important to point out that these relationships were derived using only the outer portion of Johnston's model, which is equivalent to assuming that the profile $w(u)$ is linear in the hodograph plane. Obviously, the hypothesis of linearity is wrong near the wall because of the no-slip condition, but the concerned region is very thin. Cousteix and Houdeville claim that the resulting error in the estimated thicknesses is negligible even if the maximum value of w occurs where u/q_e is approximately 0.6 [4]. Consequently, this approximation is expected to be valid and is unlikely to significantly affect the accuracy of the crossflow results.

Chapter 4

Numerical Scheme

4.1 Introduction

In the previous chapters, three integral equations were derived and the number of unknowns was reduced to match the number of equations. This chapter contains a description of the local discretization of Equations 2.6 and the Newton-Raphson-based technique for their solution. The coupled discrete equations are solved simultaneously along a row of cells aligned roughly perpendicular to the external-flow streamlines, and this procedure is repeated for subsequent downstream rows. Figure 4.1 depicts a row of cells and illustrates the labeling convention employed for cells and nodes in this document.

4.2 Discrete Formulation

The major steps involved in the construction of a a full set of discrete equations are described individually and then assembled in the last subsection.

4.2.1 Coordinate Systems

The basic computational element is a planar cell, individually constructed from the coordinates of the body in the global Cartesian system. Accordingly, a local Cartesian cell coordinate system can be defined as illustrated in Figure 4.2. The process of constructing these cells effectively corresponds to locally laying the surface-hugging grid

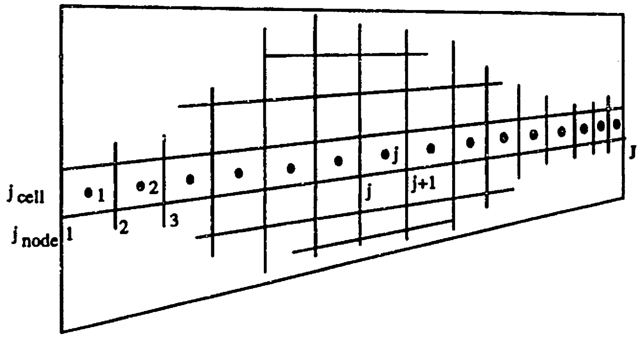

Figure 4.1: Panel and node numbering convention

out flat. A key feature of the numerical algorithm, as discussed previously, is that the surface-defining grids can be non-orthogonal.

The local cell-based coordinate system, denoted (x, z), in the current algorithm is assigned so that the z-axis is parallel to face 1-2 of the the cell, as shown in Figure 4.3. The x-axis corresponds roughly to the external streamline direction and to the solution marching direction. A right-handed coordinate system will, therefore, correspond to the y-axis pointing out of the cell.

Two additional coordinate systems are defined at each of the four nodes. The first is denoted by (s, n), and is defined by the external flow streamline at the node so that s is along the streamline direction and n is along the crossflow direction. This is the discrete version of the analytic streamline system discussed earlier. The second is defined so that at node 1, for instance, the x_1 coordinate is parallel to edge 1-4 (and the z_1 coordinate perpendicular to that). This second system is necessary only to define the direction of the external flow streamline in terms of the grid. However, in order for this second nodal system to be meaningful, the geometry of the surface cell adjacent to edge 3-4 also has to be defined in the coordinate system of the primary cell (bounded by nodes 1,2,3 and 4).

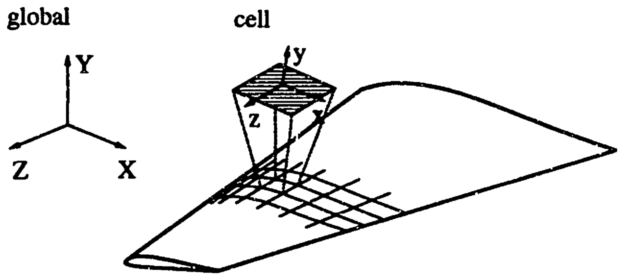

Figure 4.2: Global and cell coordinate systems

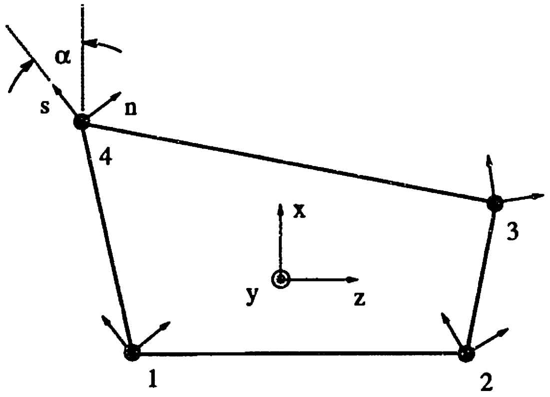

Figure 4.3: Cell and nodal streamline coordinate systems

4.2.2 Rotational Transformations

The empirical relationships of Chapter 3 are only applicable in the (s, n) coordinate system. The variables thus determined at each of the four nodes have to be rotated into the common cell coordinate system for inclusion in the discretized equations.

Following the convention of considering counterclockwise angles positive, transformation relations for a generic rotation α are readily obtained by substituting the rotated velocity components $(\tilde{u}, \tilde{w})$,

$$\begin{pmatrix} \tilde{u} \\ \tilde{w} \end{pmatrix} = \begin{pmatrix} \cos(\alpha) & -\sin(\alpha) \\ \sin(\alpha) & \cos(\alpha) \end{pmatrix} \begin{pmatrix} u \\ w \end{pmatrix},$$

into the variable definitions. The resulting relations are listed below.

$$\begin{aligned}
\delta_1^* &= \cos(\alpha)\,\delta_x^* - \sin(\alpha)\,\delta_z^* \\
\delta_2^* &= \sin(\alpha)\,\delta_x^* + \cos(\alpha)\,\delta_z^* \\
\theta_1^* &= \cos(\alpha)\,\theta_x^* - \sin(\alpha)\,\theta_z^* \\
\theta_2^* &= \sin(\alpha)\,\theta_x^* + \cos(\alpha)\,\theta_z^* \\
\delta_1^{**} &= \cos(\alpha)\,\delta_x^{**} - \sin(\alpha)\,\delta_z^{**} \\
\delta_2^{**} &= \sin(\alpha)\,\delta_x^{**} + \cos(\alpha)\,\delta_z^{**} \\
\theta_{11} &= \cos^2(\alpha)\,\theta_{xx} + \sin^2(\alpha)\,\theta_{zz} - \cos(\alpha)\,\sin(\alpha)\,\left(\theta_{xz} + \theta_{zx}\right) \\
\theta_{22} &= \sin^2(\alpha)\,\theta_{xx} + \cos^2(\alpha)\,\theta_{zz} + \cos(\alpha)\,\sin(\alpha)\,\left(\theta_{xz} + \theta_{zx}\right) \\
\theta_{12} &= \cos^2(\alpha)\,\theta_{xz} - \sin^2(\alpha)\,\theta_{zx} + \cos(\alpha)\,\sin(\alpha)\,\left(\theta_{xx} - \theta_{zz}\right) \\
\theta_{21} &= \cos^2(\alpha)\,\theta_{zx} - \sin^2(\alpha)\,\theta_{xz} + \cos(\alpha)\,\sin(\alpha)\,\left(\theta_{xx} - \theta_{zz}\right)
\end{aligned}$$

Rotation of all vector quantities into the local cell system before differencing properly accounts for the grid non-orthogonality. These transformations are effectively equivalent to adding the necessary metric-gradient terms that arise when the equations are written for a general curvilinear coordinate system.

4.2.3 Derivative Terms

The derivative terms are discretized using Green's theorem,

$$\oint_c P\,dz = -\iint_S \frac{\partial P}{\partial x}\,dS$$

and

$$\oint_c Q\,dx = \iint_S \frac{\partial Q}{\partial z}\,dS\,,$$

where $P(x,z)$ and $Q(x,z)$ are continuous functions and have continuous first order partial derivatives in a region, S. The first order derivative terms in Equations 2.6 on a cell of area S are, therefore, approximated by

$$\frac{\partial P}{\partial x} = -\frac{1}{S}\left[\frac{(P_1+P_2)}{2}\Delta z_{21} + \frac{(P_2+P_3)}{2}\Delta z_{32} + \frac{(P_3+P_4)}{2}\Delta z_{43} + \frac{(P_4+P_1)}{2}\Delta z_{14}\right]$$

and

$$\frac{\partial Q}{\partial z} = \frac{1}{S}\left[\frac{(P_1+P_2)}{2}\Delta x_{21} + \frac{(P_2+P_3)}{2}\Delta x_{32} + \frac{(P_3+P_4)}{2}\Delta x_{43} + \frac{(P_4+P_1)}{2}\Delta x_{14}\right]\,,$$

where the face lengths

$$\Delta z_{21} = z_2 - z_1$$
$$\Delta z_{32} = z_3 - z_2$$
$$\Delta z_{43} = z_4 - z_3$$
$$\Delta z_{14} = z_1 - z_4$$
$$\Delta x_{21} = x_2 - z_1$$
$$\Delta x_{32} = x_3 - z_2$$
$$\Delta x_{43} = x_4 - z_3$$
$$\Delta x_{14} = x_1 - z_4$$

are defined in a counterclockwise direction. The numeric subscripts refer to the nodes in Figure 4.3. The area S is calculated by

$$S = \frac{1}{2}\left(\Delta z_{31}\Delta x_{42} - \Delta z_{42}\Delta x_{31}\right) .$$

4.2.4 Odd-Even Decoupling and Source Terms

The finite-volume box scheme developed here is equivalent to central–differencing the derivative terms along the considered row of cells on a uniform Cartesian mesh. Hence, given that the analytic equations have no intrinsic dissipation terms, the numerical scheme permits sawtooth oscillations in the solution which not only mask the physics of the flow but also cause substantial stability problems.

The problem of saw-tooth modes is largely rectified by weighting or biasing the values of variables at each of the four nodes in the evaluation of the source terms in Equations 2.6 on a cell. (This is achieved at the expense of some formal numerical accuracy.) For instance, the displacement thickness is calculated from

$$\delta_x^* = (1-\eta)\left[(1-\lambda)\,\delta_{x_1}^* + \lambda\,\delta_{x_2}^*\right] + \eta\left[\lambda\,\delta_{x_3}^* + (1-\lambda)\,\delta_{x_4}^*\right] ,$$

where η and λ control the weighting in the x and z directions, respectively. The formulation of biasing in this manner is consistent because the sum of the coefficients at each of the four nodes is unity.

A demonstration of the effectiveness of source-term weighting in mitigating sawtooth modes is provided in Figures 4.4 and 4.5. The associated cause will become evident in the section on Jacobian-matrix structure.

4.2.5 Local Construction of Discrete Equations

Each row of cells is solved separately, as indicated earlier. For each of these rows, the constituent cells are visited individually at each iteration and a cell residual-vector, $\boldsymbol{R}$,

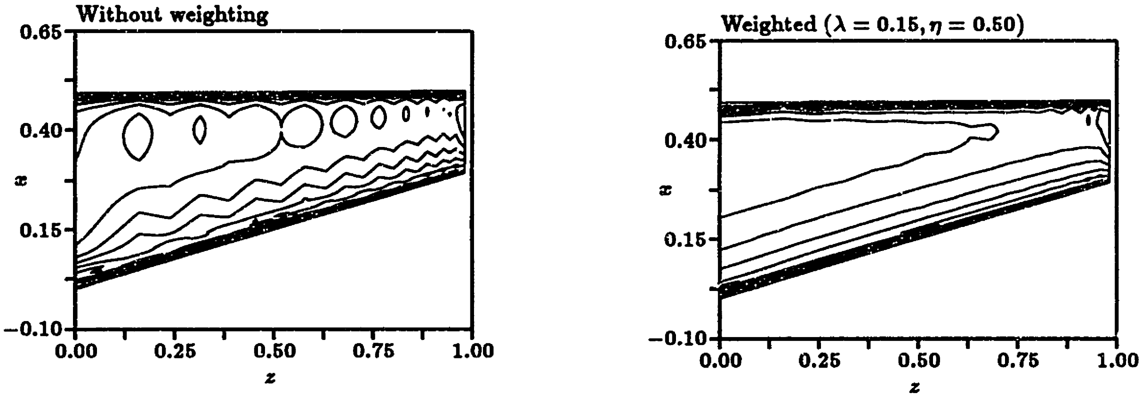

Figure 4.4: The effect of source-term weighting on the distribution of H

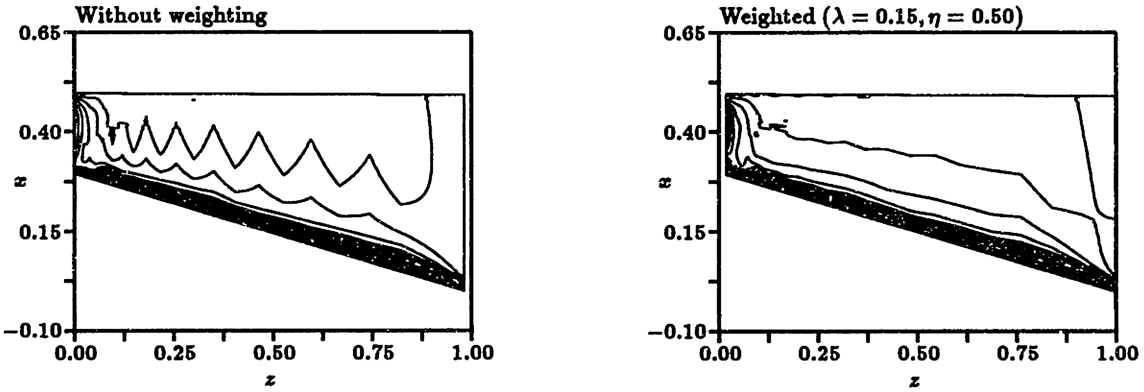

Figure 4.5: The effect of source-term weighting on the distribution of β_w

is constructed. The individual procedures involved, described in the preceding sections, are assembled here. The method developed in this thesis is a box scheme; the solution is, therefore, stored at the four nodes. The scheme is formally second-order accurate in space with no source-term weighting.

The vector of primary variables, $\boldsymbol{U}$, is known at nodes 1 and 2 from the solution at the previous upstream row. The values at nodes 3 and 4 are unknown. In OMAR, they are initialized to be those at nodes 1 and 2 respectively, recognizing that these values are all in the local (s, n) coordinate system.

The procedure employed at each of the nodes at a cell is as follows. First, the closure formulae are applied to determine all the non-primary unknowns from $\boldsymbol{U}$, in the (s, n) system. Next, these unknowns are rotated into (x, z) coordinates. Then, in Equations 2.6, which are reproduced below for convenience, the derivative terms are approximated by the finite-volume method of § 4.2.3 and the source terms are evaluated as described in § 4.2.4. The derivatives of velocities are also evaluated as described in § 4.2.3 from their known components in the (x, z) system at the nodes and then simply multiplied to the remaining source-term cell-averaged variables.

$$\frac{\partial}{\partial x}\left(\rho_e q_e^2 \theta_{xx}\right) + \frac{\partial}{\partial z}\left(\rho_e q_e^2 \theta_{xz}\right) + \rho_e q_e \delta_x^* \frac{\partial u_e}{\partial x} + \rho_e q_e \delta_z^* \frac{\partial u_e}{\partial z} = \tau_{x_w}$$

$$\frac{\partial}{\partial x}(\rho_e q_e^2 \theta_{zx}) + \frac{\partial}{\partial z}(\rho_e q_e^2 \theta_{zz}) + \rho_e q_e \delta_x^* \frac{\partial w_e}{\partial x} + \rho_e q_e \delta_z^* \frac{\partial w_e}{\partial z} = \tau_{z_w}$$

$$\frac{\partial}{\partial x}(\rho_e q_e^3 \theta_x^*) + \frac{\partial}{\partial z}(\rho_e q_e^3 \theta_z^*) + \rho_e q_e \delta_x^{**} \frac{\partial q_e^2}{\partial x} + \rho_e q_e \delta_z^{**} \frac{\partial q_e^2}{\partial z} = 2D$$

The system of three discrete equations, thus developed, can be expressed as a function of the unknowns by writing the residual vector $\boldsymbol{R}$ as a function of $\boldsymbol{U}$ at the two downstream nodes 3 and 4,

$$\boldsymbol{R}(\boldsymbol{U}_3, \boldsymbol{U}_4) = \boldsymbol{R}\left((\theta_{11})_3, \tan(\beta_w)_3, (\delta_1^*)_3, (\theta_{11})_4, \tan(\beta_w)_4, (\delta_1^*)_4\right) = 0\,. \qquad (4.1)$$

4.3 Initial Condition

The term initial condition is used by analogy to the corresponding time-marching scheme. For the boundary layer, an initial condition needs to be prescribed along the first row of cells to start the calculation. In general, fluid has to be entering the calculation domain along this initial row of cells to satisfy the characteristic direction requirement. Usually, in calculations performed to compare with experimentally-obtained results, the initial condition is provided by the experiment. This is the case with the first set of results in this thesis.

For a wing calculation, the initial condition can be generated by solving the attachment line equations. For turbulent flow, this is an involved effort (see, for example, Cumpsty and Head [5]). In OMAR, the initial condition is prescribed from the solution of the incompressible equations for laminar flow using Falkner-Skan profiles to generate a value for δ_1^* at the nodes on either side of the attachment line [3]. The assumption that the flow is locally identifiable with the flow on the leading edge of an equivalent infinite swept wing is made. In addition, a value for H is specified to yield the initial condition for θ_{11}, while the initial value of β_w is approximated to be zero. This process only requires $\partial u_e/\partial n$ at the attachment line and the laminar viscosity μ as inputs. While this approach yields slightly inaccurate initial conditions, it is still employed because, even for very high freestream Reynolds numbers, $Re_{\theta_{11}}$ is very low near the attachment line. Furthermore, the strong favorable pressure gradient which exists just downstream will tend to make conditions over the major part of the wing comparatively insensitive to conditions on the attachment line [5].

4.4 Boundary Conditions

Boundary conditions can be applied along the two sides of the domain parallel to the marching direction. The boundary condition along the remaining side was discussed in the previous section.

Along a row of N cells, there are 3N+3 primary unknowns but only 3N discrete equations. Therefore, three additional equations need to be supplied. This requirement is merely a numerical consequence and is distinct from physical issues although, as will be discussed shortly, the location of the application of these additional equations is subject to the flow solution.

The requirement for the additional equations is fulfilled by the specification of boundary conditions. While the numerical scheme allows a generous latitude in the nature of these conditions, one particular type is empirically found to be most suitable for the generic case.

In general, simple Dirichlet boundary conditions are found to trigger large-amplitude saw-tooth modes in the solution. Therefore, despite their obvious utility in cases where the physical state of the boundary layer at the edge of the domain is known, they are not considered here. Similarly, Neumann boundary conditions of the type where a certain gradient is enforced also usually excite saw-tooth oscillations. The most successful boundary conditions tested are those where the edge node is simply extrapolated from the two adjacent interior nodes. These will be referred to as zero-curvature Neumann conditions. For instance, the displacement thickness at the boundary is calculated from $\delta^*_{1_J} = 2\delta^*_{1_{J-1}} - \delta^*_{1_{J-2}}$. Of all the various types tried, zero-curvature boundary conditions are empirically found to least excite saw-tooth modes. Figure 4.6 shows the dramatic difference in the solution when zero-curvature conditions are applied instead of zero-gradient ones.

Following the discussion in § 2.4, it is clear that domains of influence and dependence dictate the application of boundary conditions along those edges of the domain where characteristic directions indicate the passage of information into the domain. In principle, as many boundary conditions as their are characteristics crossing the boundary are required. A corollary to this is that in regions where characteristics indicate that information is outbound, no conditions are needed; if any are applied, they will exert no influence on the solution in the interior of the domain.

Boundary conditions should ideally be in a form where the values of the characteris-

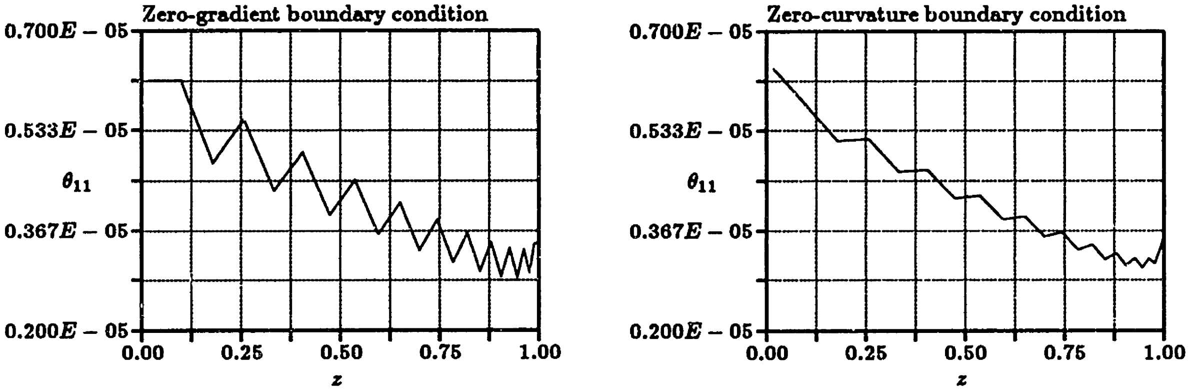

Figure 4.6: Comparison of zero-gradient and zero-curvature boundary conditions

tics are enforced depending on their directions relative to the domain boundary. Clearly, specifying all three characteristics is equivalent to specifying $\boldsymbol{U}$. Situations where, at a boundary, some characteristics are outbound and others inbound are expected to be infrequent and transitory. Enforcing $\boldsymbol{U}$ in such situations is, therefore, found to be justified. It is sensible to prescribe either all three primary variables, or none at all, regardless of the number of inbound or outbound characteristics. This is not a problem in practice.

The effect of boundary conditions on the solution is limited to regions bounded by the path traced by the most angularly-directed characteristic, by virtue of the existence of a domain of influence.

In OMAR, zero-curvature boundary conditions are applied at both side boundaries, unless otherwise specified. Three extra equations replace the three residual vector components at one end of the row of cells.

4.5 Solution Method

The previous section described the construction of the system of discrete Equations 4.1 for a row of cells in terms of $\boldsymbol{U}$ at the downstream nodes. This system is solved in OMAR using the well-known Newton-Raphson method.

4.5.1 Newton-Raphson Method

The basic Newton-Raphson method for a system of non-linear equations is exactly analogous to its scalar analog. The vector of equations $\boldsymbol{F}$

$$\boldsymbol{F}(\boldsymbol{V}) = 0\,,$$

is solved where $\boldsymbol{V}$ is the vector of unknowns. At the m^{th} iteration level, the Newton-Raphson solution procedure is

$$\left[\frac{\partial \boldsymbol{F}}{\partial \boldsymbol{V}}\right]^m \delta \boldsymbol{V}^m = -\boldsymbol{F}^m\,.$$

The variables at the next iteration level are simply updated

$$\boldsymbol{V}^{m+1} = \boldsymbol{V}^m + \delta \boldsymbol{V}^m\,,$$

where

$$\delta \boldsymbol{V}^m = -\left[\frac{\partial \boldsymbol{F}}{\partial \boldsymbol{V}}\right]^{m^{-1}} \boldsymbol{F}^m\,.$$

These updates can be under-relaxed for strongly non-linear equations. The Jacobian matrix $\left[\frac{\partial \boldsymbol{F}}{\partial \boldsymbol{V}}\right]^m$ must be computed and inverted for each Newton-Raphson step. This system represents the partial derivative of each of the equations in the vector $\boldsymbol{F}$ with respect to each of the variables in $\boldsymbol{V}$.

4.5.2 Jacobian-Matrix Structure

An interior row of the Jacobian-matrix consists of two blocks. Each block is a 3×3 matrix representing the sensitivity of the vector of residuals at a cell $\boldsymbol{R}_j$ to the vector of primary unknowns $\boldsymbol{U}_j$ at either node j or node j+1,

$$\left[\frac{\partial \boldsymbol{R}}{\partial \boldsymbol{U}}\right]_j = \begin{bmatrix} \frac{\partial R_1}{\partial \theta_{11}} & \frac{\partial R_1}{\partial \tan(\beta_w)} & \frac{\partial R_1}{\partial \delta_1^*} \\ \frac{\partial R_2}{\partial \theta_{11}} & \frac{\partial R_2}{\partial \tan(\beta_w)} & \frac{\partial R_2}{\partial \delta_1^*} \\ \frac{\partial R_3}{\partial \theta_{11}} & \frac{\partial R_3}{\partial \tan(\beta_w)} & \frac{\partial R_3}{\partial \delta_1^*} \end{bmatrix}_{j \text{ or } j+1} .$$

Each element of the 3×3 block is constructed from individual components using the chain rule. In order to illustrate this, an overbar notation is introduced first for convenience to denote the residual written in terms of less fundamental constituents. Then, using the first component of $\boldsymbol{R}$, for instance,

$$R_1 = R_1(\boldsymbol{U}_4, \boldsymbol{U}_3) = \overline{R_1}(\theta_{xx_4}, \theta_{xx_3}, \theta_{xz_4}, \theta_{xz_3}, \delta_x^*, \delta_z^*, c_{f_w}) ,$$

the Jacobian is constructed as follows:

$$\left[\frac{\partial R_1}{\partial \theta_{11}}\right]_4 = \left[\frac{\partial \overline{R_1}}{\partial \theta_{11}}\right]_4 + \left[\frac{\partial \overline{R_1}}{\partial \theta_{12}}\frac{\partial \theta_{12}}{\partial \theta_{11}}\right]_4 + \left[\frac{\partial \overline{R_1}}{\partial \theta_{21}}\frac{\partial \theta_{21}}{\partial \theta_{11}}\right]_4 + \left[\frac{\partial \overline{R_1}}{\partial \theta_{22}}\frac{\partial \theta_{22}}{\partial \theta_{11}}\right]_4$$
$$+ \left[\frac{\partial \overline{R_1}}{\partial \delta_2^*}\frac{\partial \delta_2^*}{\partial \theta_{11}}\right]_4 + \left[\frac{\partial \overline{R_1}}{\partial c_{f_1}}\frac{\partial c_{f_1}}{\partial \theta_{11}}\right]_4 + \left[\frac{\partial \overline{R_1}}{\partial c_{f_2}}\frac{\partial c_{f_2}}{\partial \theta_{11}}\right]_4$$

In the expression above, some derivatives are related to empirical relationships, for example $\partial \theta_{12}/\partial \theta_{11}$. These are also constructed using a series of chain rules. An example of the construction of the other kind of derivative is

$$\frac{\partial \overline{R_1}}{\partial \theta_{12}} = \frac{\partial \overline{R_1}}{\partial \theta_{xx}}\frac{\partial \theta_{xx}}{\partial \theta_{12}} + \frac{\partial \overline{R_1}}{\partial \theta_{xz}}\frac{\partial \theta_{xz}}{\partial \theta_{12}} .$$

Here, derivatives of the type $\partial \theta_{xx}/\partial \theta_{12}$ are obtained from the rotational transformations.

All Jacobian-matrix elements are assembled at the FORTRAN level within OMAR through simple multiplication and addition of constituent elements. Such an approach simplifies program debugging and provides a framework for readily incorporating changes, for example in empirical relations, in future versions of the code.

The discretization scheme results in a Jacobian matrix that is bidiagonal in the interior of a row. Therefore, the matrix can be structured so that either the upper or

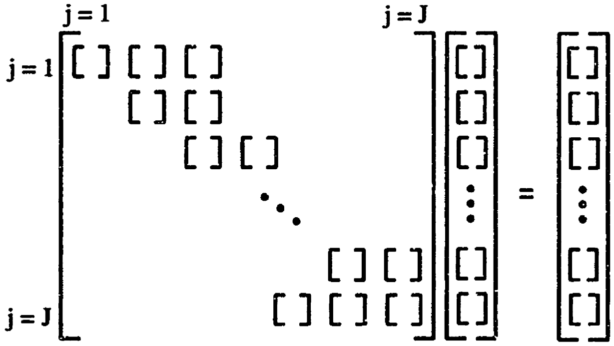

Figure 4.7: Upper-diagonal Jacobian-matrix structure

lower diagonal can be employed. The two possibilities are illustrated in Figures 4.7 and 4.8. The structure in both cases is recognized to contain the zero-curvature type boundary condition applied at both ends of the row. One set of residual equations at either edge cell is overwritten by one set of the boundary conditions.

The efficacy of source-term weighting in suppressing saw-tooth modes can be understood in terms of the Jacobian-matrix structure. In the case of the upper diagonal being filled, assigning a value less than 0.5 to λ results in increasing the diagonal dominance of the matrix. Similarly, a value greater than 0.5 increases the diagonal dominance of the lower-diagonal matrix. On the other hand, assigning to η a value greater than 0.5 increases the norm of the Jacobian matrix but does not significantly affect its diagonal dominance. Therefore, biasing η is not expected to affect the appearance of saw-tooth modes in the solution. This expectation is empirically confirmed.

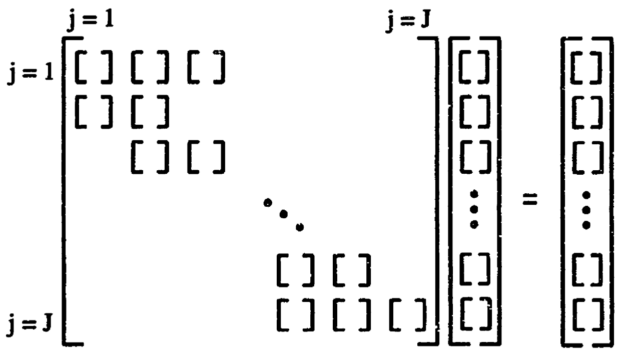

Figure 4.8: Lower-diagonal Jacobian-matrix structure

Chapter 5

Results and Discussion

Some results from two calculations are presented in this chapter. The first was performed to simulate a quasi-two-dimensional flow. The primary intention was to compare the computed results with a well-known experiment in order to ascertain the veracity of the employed empirical closure. The latter calculation was performed over a finite swept tapered wing mainly to demonstrate OMAR's three dimensional capabilities.

5.1 An Infinite Swept Wing

5.1.1 Overview

The experimental results presented here were obtained on an "infinite swept wing" under incompressible flow conditions [17]. The experiment was conducted by van den Berg and Elsenaar at The Netherland's National Aerospace Laboratory in 1972 [17].

The wing is actually a flat plate with an adverse pressure distribution induced on it by a suitably-shaped body positioned near the plate. The experiment was designed so that, over the forward portion of the experimental model, the pressure remained nearly constant before being made to increase gradually through the presence of the body. The pressure-gradient and sweep combine to induce three-dimensional separation in the vicinity of the trailing edge.

Considerable care was exercised in the attempt to simulate infinite-wing conditions. The boundary layer could be maintained very nearly quasi-two-dimensional with the help of guide vanes on either side of the region of interest. The positions of the measurement stations relevant to this calculation are depicted on the experimental model along with other notable features in Figure 5.1. The line of equally-spaced measurement stations was 0.90 m long. The angle of sweep of the wing was 35^o.

Detailed measurements and descriptions of the experimental techniques are provided by the authors. This experiment has been extensively used to compare details of closure assumptions in many different kinds of numerical methods [4, 14, 18].

5.1.2 Calculation Details

The calculation was performed on a 200×3 grid assuming quasi-two-dimensional flow. One set of grid-lines was parallel to the freestream direction and the other to the wing leading edge. The computational domain corresponded to the region enclosed by stations 1 and 10 in the experiment.

A cubic spline-interpolation technique was employed to smooth the supplied external velocity measurements required as an input to OMAR. Figure 5.2 is a vector plot of the velocity field. The spanwise component of velocity gradually increases downstream.

The initial condition used was the set of experimentally-obtained values at the first station. A simple zero-gradient boundary condition along the wing isobars, and thus one set of grid lines, was enforced along the side of the computational domain with the inflow. The use of this boundary condition meant that the Jacobian matrix could be efficiently inverted by the established method for block-tridiagonal matrices.

The calculation was performed in the incompressible mode; the Mach number was set to zero in the empirical relations.

5.1.3 Comparisons with Experimental Measurements

The computed results are presented in Figures 5.3 to 5.7 as the solid line. The marching coordinate has been scaled by a length of 1 m which is on the order of the

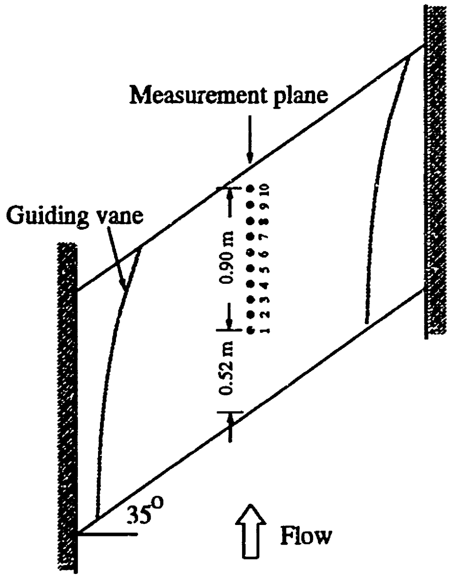

Figure 5.1: Schematic of van den Berg/Elsenaar experimental setup

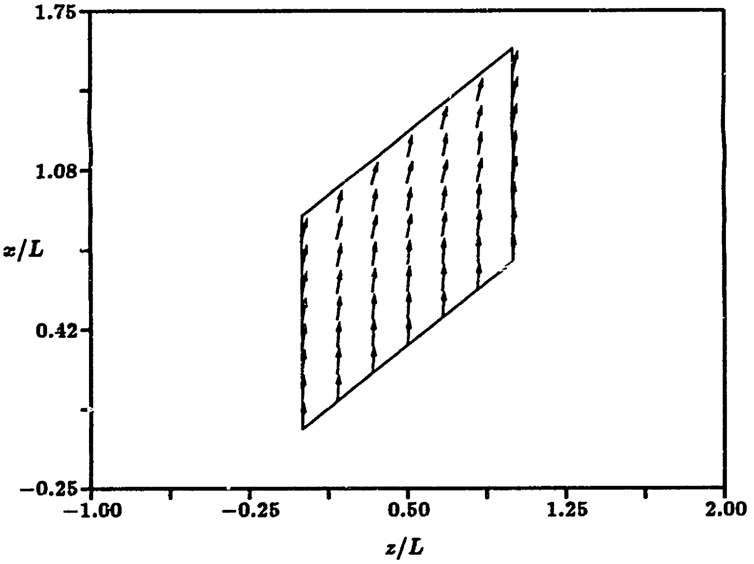

Figure 5.2: External-velocity vector plot

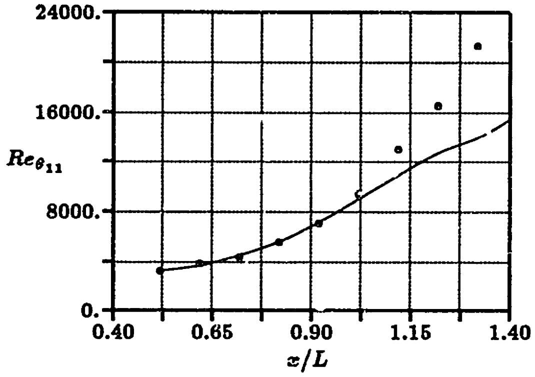

Figure 5.3: Computed variation of Reynolds number

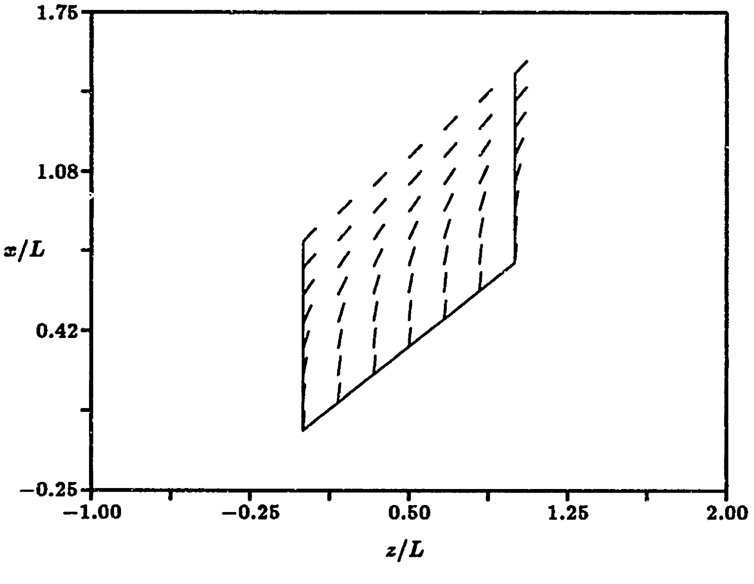

Figure 5.4: Computed limiting-streamline vector plot

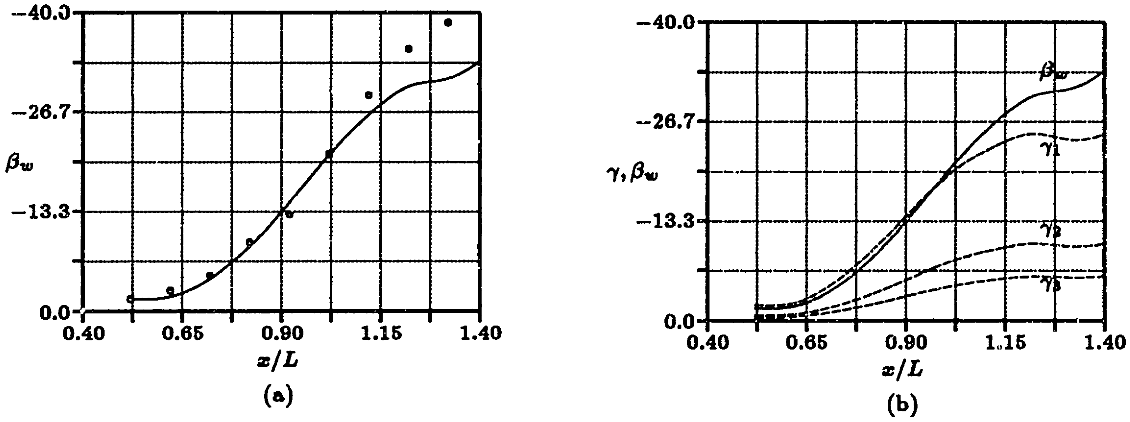

Figure 5.5: Computed variation of limiting-streamline and characteristic angles

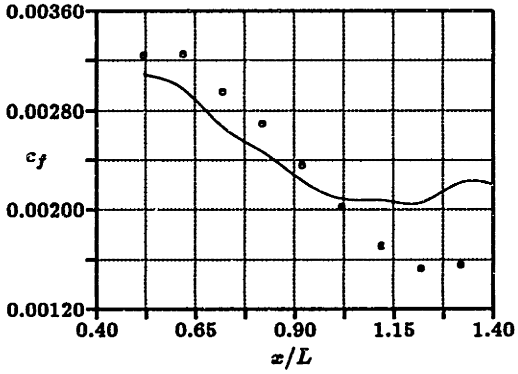

Figure 5.6: Computed variation of skin friction

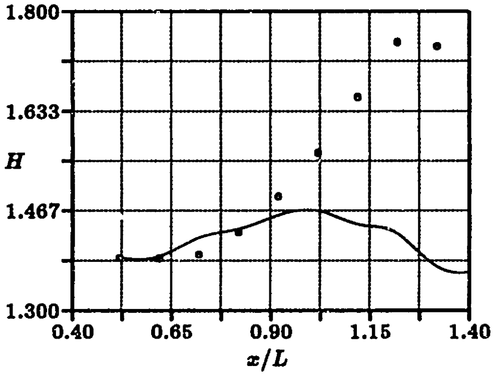

Figure 5.7: Computed variation of shape factor

wing chord.

The comparison for $Re_{\theta_{11}}$ is good up to the station near $x/L \approx 1.0$, where the spanwise flow is still a small fraction of the flow in the marching direction. This is also the case with the comparison for β_w. The negative value of β_w indicates that the limiting streamlines are turning spanwise faster than the external flow streamlines with marching distance. The tuft plot in Figure 5.4 vividly illustrates this turning. The calculated three-dimensional separation line occurs where the limiting streamlines coalesce and this is found to be close to the experimentally observed location. Experimentally, separation is observed between stations 8 and 9, or where $x/L \approx 1.3$. Figure 5.5 (b) is a plot of the variation of the three calculated characteristic directions, shown in broken lines, juxtaposed against the solid line for β_w. The three characteristic lines are observed to be oriented largely within the angular limits defined by the external flow streamline (β_w, $\gamma = 0$) and the limiting wall streamline. Furthermore, the line labeled γ_1 is evidently that associated with the limiting wall streamline.

The computed values of c_f and H compare less favorably with the experimental data. However, their values relative to experiment are consistent with one another: where c_f is under-predicted, H is over-predicted. The trend of c_f closely follows that of other published numerical case studies, employing equilibrium closure, for the same experiment [14, 18]. Comparisons are good to $x/L \approx 1.0$ but almost universally poor beyond, providing strong evidence for the widely-acknowledged inadequacy of equilibrium closure for situations with separation and large crossflow.

5.2 A Finite Swept Tapered Wing

5.2.1 Overview

The development of a compressible boundary layer over a finite tapered swept wing, at the moderate angle of attack of 1.5° and a Mach number of 0.3, was calculated to demonstrate the full three-dimensional capabilities of OMAR. The wing section was a NACA 0012 airfoil. The external inviscid velocity and density distributions, required as inputs in OMAR, are supplied by a potential flow solver [11].

The calculation was performed at a large Reynolds number to ensure that the solution throughout the domain was within the range imposed by the turbulent-flow empirical relations.

While the computed results are not compared with experiment, they are nevertheless found to be physically realistic. Comparison with experiment was precluded by the sheer volume of data that would have been required for a calculation of this nature. Furthermore, most of the external flow data available in the literature are in terms of pressure coefficients and currently, OMAR only has the ability to handle velocities as inputs.

For clarity, the graphical presentation that follows has been organized in a concise and consistent format; the lower-surface distributions are shown on the left and the upper-surface ones are shown on the right.

5.2.2 Calculation Details

The wing-surface meshes are defined by the inviscid solution and are shown in Figure 5.8. The meshes on the upper and lower surfaces are identical, measuring 57×23, with the greater number of nodes in the chordwise direction.

The boundary-layer computations were performed independently on the upper and

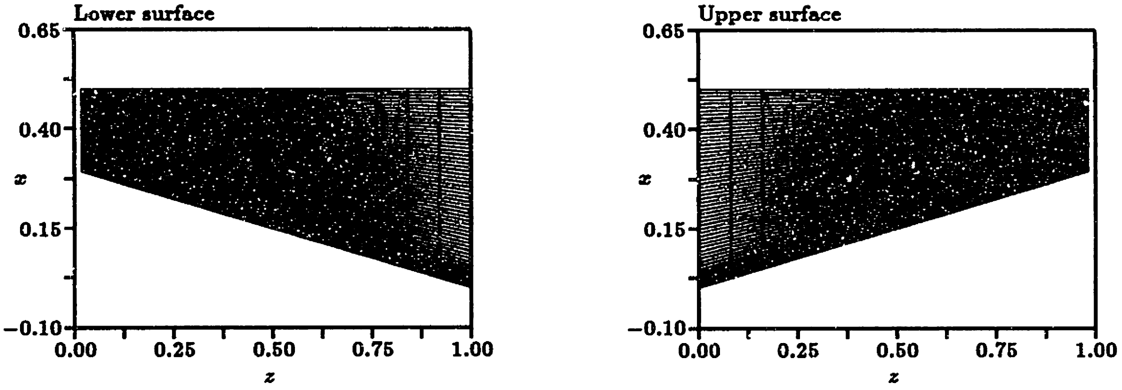

Figure 5.8: Plots of finite-wing computational meshes

lower surfaces. The actual tip of the wing was neglected in both cases because of the large curvature and so no attempt was made to link the two computations along that row. The practice of referring to the tip-most row of nodes as the tip will, nevertheless, be employed in the presentation of the results.

It is important to note that the global z-coordinate direction on the lower surface is opposite to that on the upper surface. This is necessitated by the convention that the y-coordinate increase in the direction, normal to the surface, on the side with the flow. All coordinates are normalized using the wingspan.

The inviscid speed and density distributions used as external-flow inputs in the calculation are shown in Figures 5.10 and 5.9 as contour plots. Both variables have been normalized against their freestream magnitudes. The inviscid velocity is also shown as a vector plot (at only a selected number of nodes to avoid unnecessary cluttering) in Figures 5.11. It is seen that the external flow is nominally two-dimensional over most of the wing except in the leading edge and tip regions, where the spanwise components of velocity are significant.

The calculation is performed for a freestream Reynolds number, based on the mid-wing chord, Re_c, of 175×10^6. The typical magnitude of Re_c for a large transport aircraft in cruise is about 50×10^6 and the flow, under these conditions, is usually turbulent over the entire wing surface. The abnormally large Reynolds number employed for this calculation was necessary because the method employed to generate the initial condition

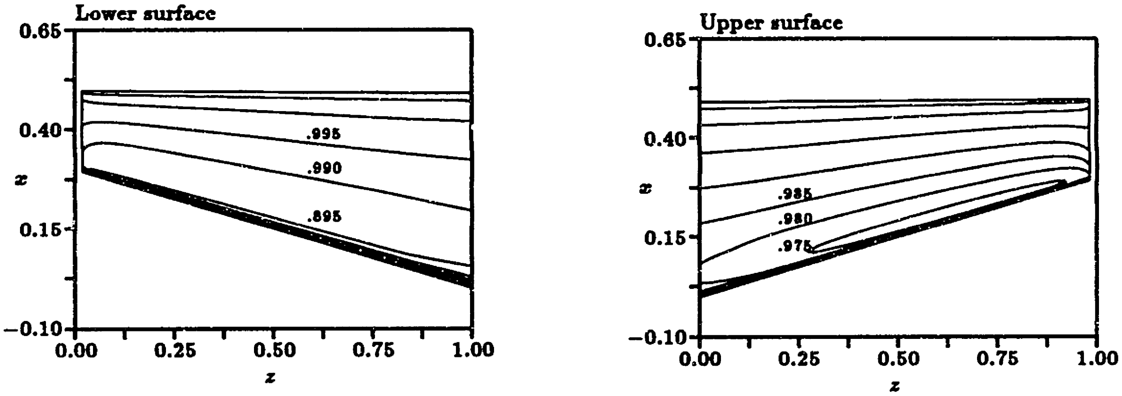

Figure 5.9: External-density contour plots

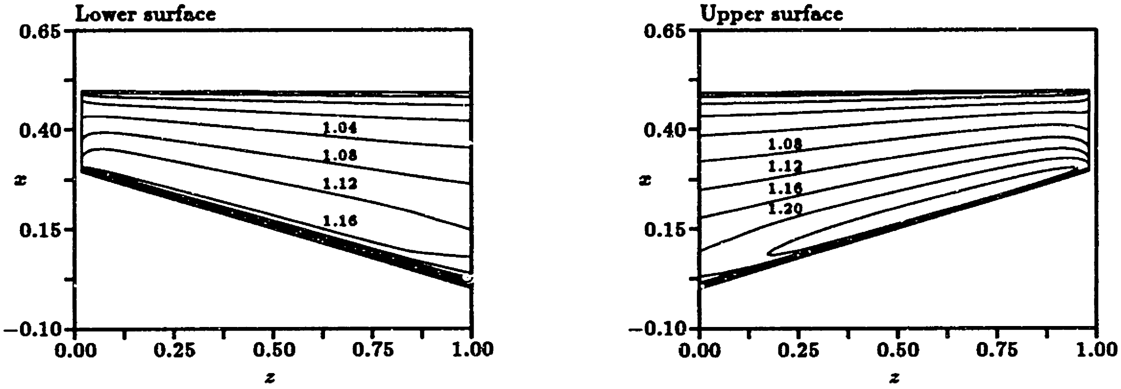

Figure 5.10: External-speed contour plots

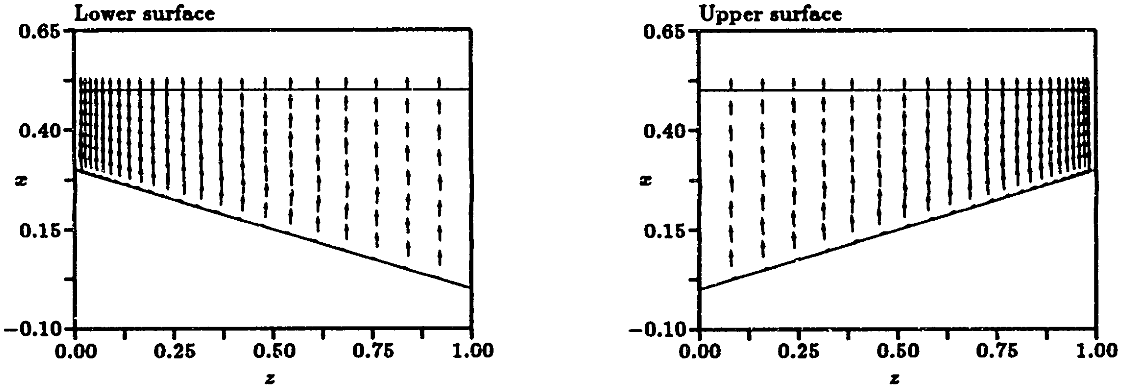

Figure 5.11: External-velocity vector plots

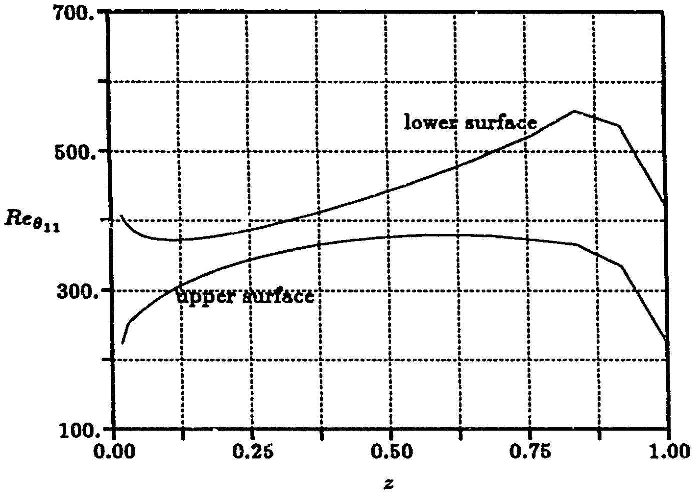

Figure 5.12: Spanwise variation of initial Reynolds number

(see § 4.3) yielded values of $Re_{\theta_{11}}$, near the attachment line, too low to sustain turbulent flow at an Re_c of 50×10^6. Such an initial condition would thus have been out of range of the empirical correlations. The initial conditions corresponding to an Re_c of 175×10^6, along the gridlines on either side of the attachment line, are shown in Figure 5.12. For the upper surface, it is seen that $Re_{\theta_{11}}$ is barely in the range considered necessary for turbulent flow.

For the initial condition calculation, the initial shape factor is specified to be 1.3. The knowledge of the location of the attachment line is required *a priori* by OMAR; in this case it lies between the row of nodes forming the leading edge and the adjacent row on the lower surface.

The restriction on Re_c is due entirely to the method employed to approximate the initial condition at the wing leading edge, and therefore will disappear with the use of a more accurate method. Furthermore, for this particular calculation, the magnitude of Re_c is not a critical issue because interest is largely confined to the qualitative performance of the method presented in this thesis.

For both surfaces, the calculations were performed with the zero-curvature boundary condition imposed at the root and at the tip. It is empirically verified that over the upper surface, a tip boundary condition is necessary to successfully compute a solution. This necessity is attributable to the characteristics crossing the domain boundaries because of the physical presence of the wing-tip vortex.

In the evaluation of the residual source terms, λ is set to 0.15 and η is kept at 0.50. The upper-diagonal Jacobian-matrix structure is used.

The residual convergence rate for each row was very high, as expected. There was a reduction of five orders of magnitude within 3 or 4 Newton-Raphson iterations. No underrelaxation was found to be necessary.

5.2.3 Computed Results

Three sets of computed results, one each for $Re_{\theta_{11}}$, β_w and H, are shown in Figures 5.13 to 5.19. Each set consists of contour plots and line plots along three chordwise stations for both the upper and lower surfaces: the root, near midwing and at the tip. In addition, for β_w "tuft" plots are shown to indicate the limiting streamline directions. Note that counterclockwise angles are considered positive.

Unlike the infinite swept wing case where a sustained adverse pressure gradient was applied to induce three-dimensional separation, it is found here that, for the Re_c considered, the flow is attached over the entire wing surface.

The boundary layer is observed to be marginally thicker on the upper surface than on the lower surface in terms of $Re_{\theta_{11}}$ near the trailing edge. In both cases, the variation is smooth and approximately two-dimensional in the direction perpendicular to the leading edges. The only notable exception appears to be in the tip region on the upper surface towards the rear of the wing. Here, the boundary layer is seen to thicken rapidly. This region also contains the large spanwise flow maintained by the wing-tip vortex.

The variation of β_w confirms that the most severe three-dimensional effects are largely restricted to areas near the leading edges and wing tips. Immediately downstream of the leading edge, drastic variations are seen. These are numerical effects,

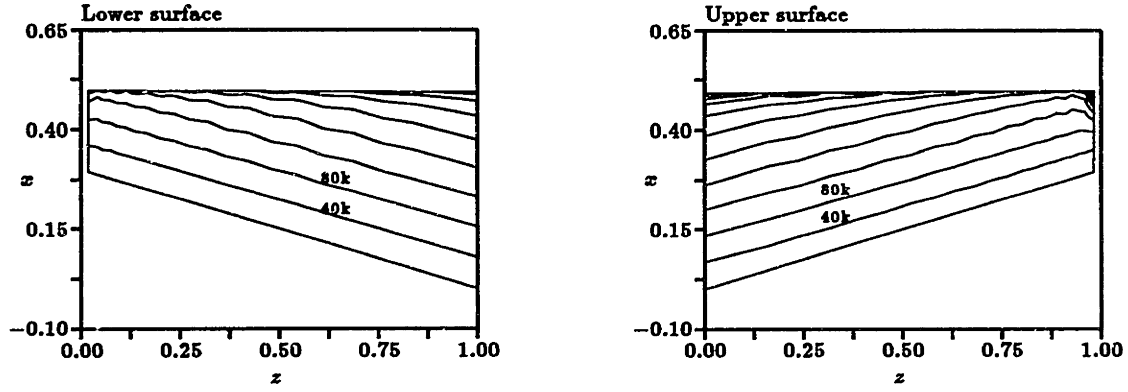

Figure 5.13: Computed Reynolds-number contour plots

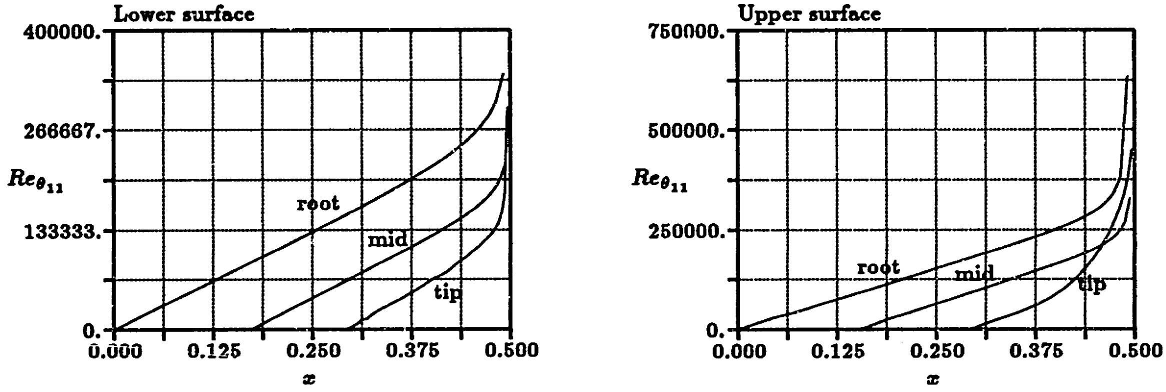

Figure 5.14: Computed Reynolds-number chordwise variation

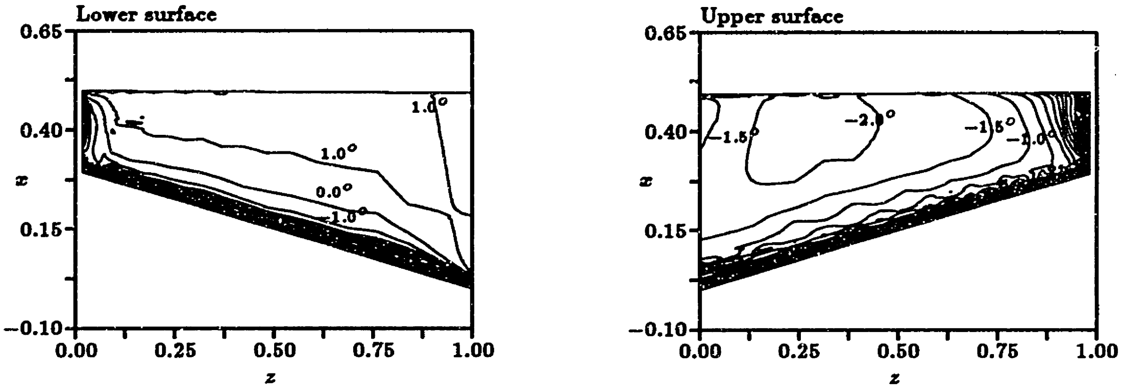

Figure 5.15: Computed limiting-streamline-angle contour plots

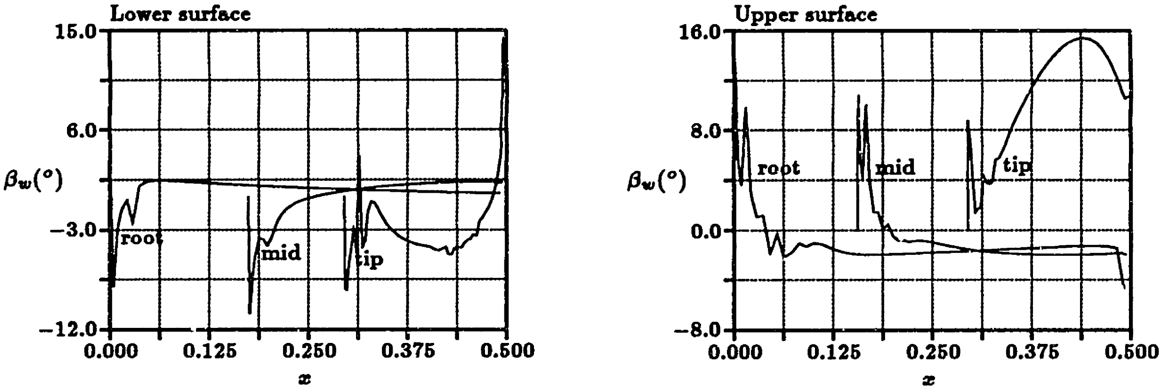

Figure 5.16: Computed limiting-streamline-angle chordwise variation

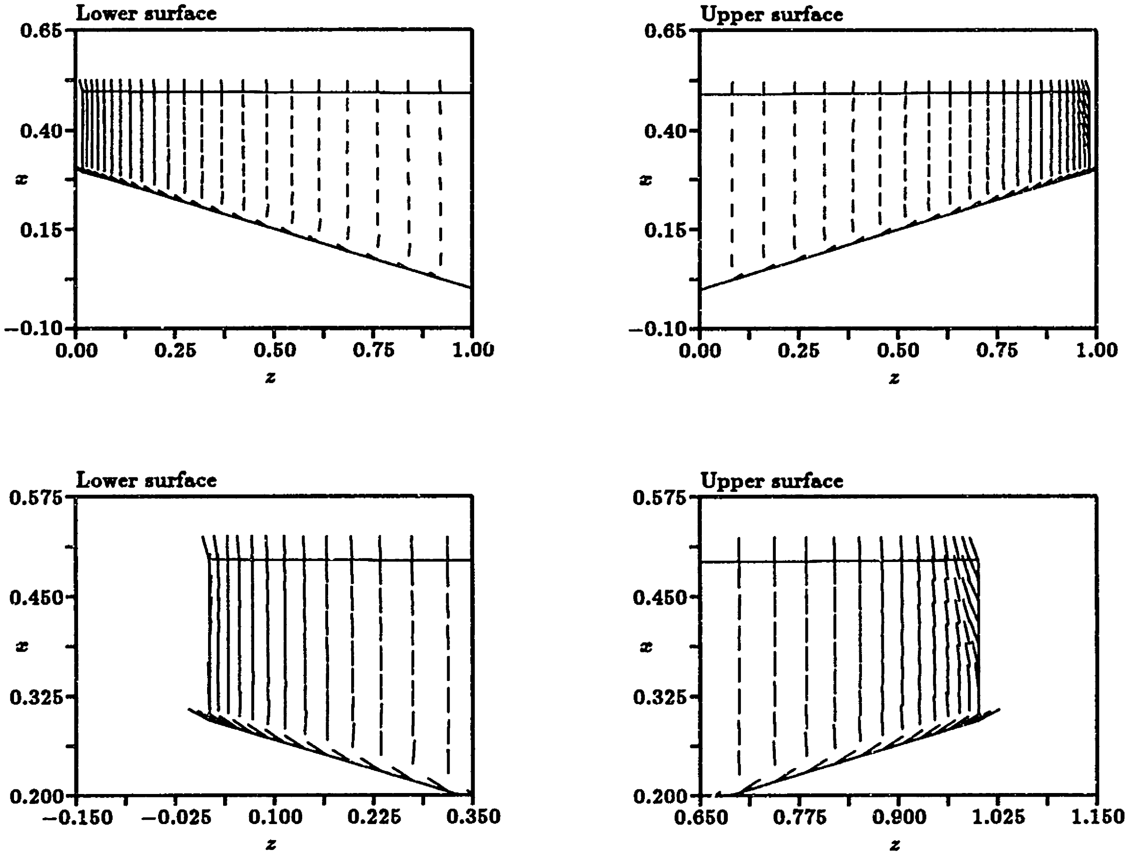
Lower surface

Upper surface

Lower surface

Upper surface

Figure 5.17: Computed limiting-streamline-angle vector plots

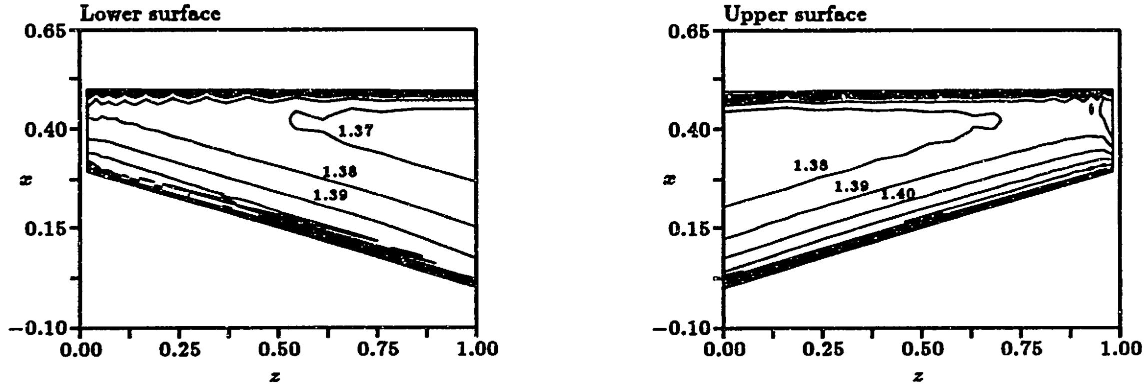

Figure 5.18: Computed shape-factor contour plots

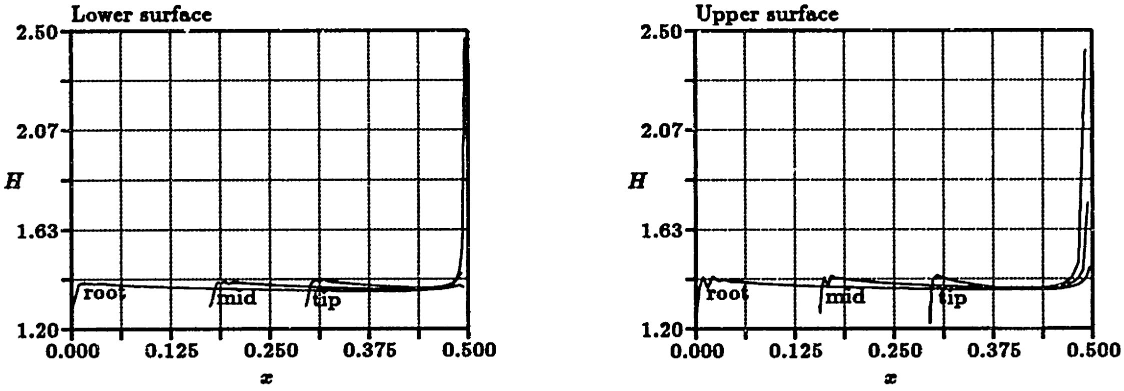

Figure 5.19: Computed shape-factor chordwise variation

presumably a consequence of the slightly incorrect initial condition for β_w, the low values of $Re_{\theta_{11}}$ and the strong pressure gradient associated with the attachment line. However, the solution quickly becomes more placid with marching distance. As noted in § 4.3, these variations are not expected to have a substantial effect on the physical accuracy of the solution over the rest of the wing.

The direction of limiting streamlines is well known to be highly responsive to the gradient of pressure. The pressure field around the wing produces three topologically distinguishable regions in terms of β_w.

The most extensive of these regions is caused by the wing sweep creating a general gradient of pressure perpendicular to the freestream direction over most of the wing. Alternatively stated, the isobar lines are swept. Here, the limiting-streamlines are directed more towards the tip than the external-flow streamlines. The magnitude of β_w is small but is, nevertheless, discernibly negative on the upper surface and positive on the lower surface.

Secondly, in the vicinity of the attachment line, the sharply decreasing pressure tends to generate large positive values of β_w on the upper surface, and large negative values on the lower surface. While these trends are initially obscured by the erratic numerical behavior over most of the span, they nevertheless seem to persist nearer the tip and are opposed by the sweep of the isobars.

Thirdly, near the tip on both surfaces, the pressure field responsible for the wing-tip vortex dominates. It is in tandem with the pressure gradient near the attachment line on the upper surface but in opposition to it on the lower surface. Consequently, on the upper surface near the leading edge and tip, there is a sharp increase in β_w to near midchord where the decreasing influence of the attachment-line results in a drop in β_w. On the lower surface, the attachment-line pressure gradient initially causes β_w to decrease but, towards the rear, the pressure field associated with the wing-tip vortex causes β_u to rise sharply.

Juxtaposed on the these last two pressure field effects is the previously-discussed influence of swept isobars. On the lower surface, the contour of zero β_w extends from the root to near the tip where it turns downstream and meets the tip near the trailing edge. This contour separates the region influenced by the attachment line from that influenced by the wing-tip vortex pressure field and swept isobars. On the upper surface, the contour of zero β_w also extends from the root to near the confluence of the tip and leading edge and then turns sharply near midchord to meet the trailing edge a significant distance away from the tip. This contour separates the region influenced by the mutually reinforcing attachment line and wing-tip vortex fields from that influenced by the swept isobar lines.

The information on the orientation of the limiting wall streamlines intrinsic in β_w is also a function of the external flow streamline directions because β_w is fundamentally defined in the streamline coordinate system. The tuft plots account for the variation in the direction of external-flow streamlines and, hence, show the physical appearance of the direction of the flow in the wall limit.

The effects of the pressure field are also manifest in the H distributions, although to a less discernible extent. The most readily observed relation between the pressure gradient and H is the two-dimensional version of separation; an adverse gradient promotes separation while a favorable gradient opposes it. Therefore, as is observable in Figures 5.18 and 5.19, regions of decreasing H correspond to favorable pressure gradients.

Chapter 6

Conclusions and Future Work

This thesis has developed a novel numerical method for solving the three-dimensional integral boundary layer equations on non-orthogonal grids. The chief singular achievement of the method is the application of a finite-volume formulation that keeps the equations independent of surface and grid metrics. This results in substantial syntactic simplification and great flexibility in the choice of grids.

The use of an integral form of the equations yields a very fast method; the calculation on the finite wing takes only about 15 seconds on a DECstation 5000. In terms of integral variables, this method is as accurate as many differential, equilibrium-closure methods reported in a recent Eurovisc-Workshop [18].

The contextual basis of this thesis, as outlined in the Chapter 1, was to develop a boundary layer method with the eventual aim of incorporating it into a viscous/inviscid code. The use of the Newton-Raphson technique is very helpful in this regard; the elements of the Jacobian-matrix can be appended to the global Jacobian matrix in a Newton-Raphson-based Full-Potential code to develop a global coupled scheme.

While this thesis presents a complete working computational method, there are nevertheless a few improvements that would enhance its robustness and place it on a less *ad hoc* basis. The most important of these is to devise a better alternative to the zero-curvature boundary conditions and source-term weighting to ameliorate odd/even decoupling. Currently, this is envisioned to be achieved by upwinding characteristic variables through an idea borrowed from the concept of retarded density in the solution of the Full-Potential equation. Such an approach would largely maintain the current computer program structure.

Improvements in the empirical correlations, especially at low $Re_{\theta_{11}}$, can be made by replacing the currently-employed correlations with more accurate ones. These can be gleaned from the emerging literature. As has already been mentioned, the structure of the program readily permits such changes. In the longer term, the equilibrium model may, perhaps, be dropped in favor of one based on a transport equation, especially if it incorporates a three-dimensional law of the wall.

The empiricisms can be easily extended to laminar flow through the assumption of Falkner-Skan streamwise and Cook crossflow profiles. This is a necessity in the wing attachment-line region to permit realistic flight Reynolds-number solutions to be computed. However, reliable transition criteria in three dimensions will then have to be devised.

Bibliography

[1] D.A. Anderson, Tannehill J.C., and Pletcher R.H. *Computational Fluid Mechanics and Heat Transfer*. Hemisphere Publishing Corporation, New York, 1984.

[2] T. Cebeci and A. M. O. Smith. *Analysis of Turbulent Boundary Layers*. Academic Press, New York, 1974.

[3] J. Cousteix. Three-dimensional boundary layers. introduction to calculation methods. In *Computation of Three-Dimensional Boundary Layers Including Separation*, Apr 1986. AGARD-R-741.

[4] J. Cousteix and R. Houdeville. Singularities in three-dimensional turbulent boundary layer calcuations and separation phenomena. *AIAA Journal*, 19(8), Aug 1981.

[5] N.A. Cumpsty and M.R. Head. The calculation of three-dimensional turbulent boundary layers. part II: Attachment-line flow on an infinite swept wing. *The Aeronautical Quarterly*, 28:150–164, 1967.

[6] M. Drela. *Two-Dimensional Transonic Aerodynamic Design and Analysis Using the Euler Equations*. PhD thesis, MIT, Dec 1985. Also, MIT Gas Turbine & Plasma Dynamics Laboratory Report No. 187, Feb 1986.

[7] J.P. Johnston. *Three-dimensional turbulent boundary layers*. PhD thesis, MIT, 1957. Also, MIT Gas Turbine Laboratory Report No. 39.

[8] A. Mager. Generalization of boundary-layer momentum integral equations to three-dimensional flows, including those of rotating systems. Technical Report 1067, N.A.C.A., 1952.

[9] D. F. Myring. An integral prediction method for three-dimensional turbulent boundary layers in incompressible flow. Technical Report 32647, Aeronautical Research Council, 1970.

[10] J.F. Nash and V.C. Patel. *Three-Dimensional Turbulent Boundary Layers.* SBC Technical Books, Atlanta, 1972.

[11] P.B. Foll. Full potential analysis and design of transonic propellers. CFDL TR-91-1, MIT, Feb 1991.

[12] G.S. Raetz. A method of calculating three-dimensional laminar boundary-layers of steady compressible flows. Technical Report NAI-58-73, Northrop Aircraft Inc., 1957.

[13] P. D. Smith. Calculation methods for three-dimensional turbulent boundary layers. R & M Report 3523, Aeronautical Research Council, HMSO, London, 1968.

[14] P. D. Smith. An integral prediction method for three-dimensional compressible turbulent boundary layers. R & M Report 3739, Aeronautical Research Council, HMSO, London, 1972.

[15] T. W. Swafford. Analytical approximation of two-dimensional separated turbulent boundary-layer velocity profiles. *AIAA Journal*, 21(6):923–926, 1983.

[16] T.W. Swafford and D.L. Whitfield. Time-dependent solution of three-dimensional compressible turbulent integral boundary-layer equations. *AIAA Journal*, 23(7):1005–1013, Jul 1985.

[17] B. van den Berg and A. Elsenaar. Measurements in a three-dimensional incompressible turbulent boundary layer in an adverse pressure gradient under infinite swept wing conditions. Technical Report NLR TR 72092U, Nationaal Lucht-En Ruimtevaartlaboratorium, Amsterdam, 1972.

[18] B. van den Berg, D.A. Humphreys, E. Krause, and J.P.F. Lindhout. Three-dimensional turbulent boundary layers – calculations and experiments. Notes on numerical fluid mechanics, Germany, 1988.

[19] K.C. Wang. On the determination of the zones of influence and dependence for three-dimensional boundary-layer equations. *Journal of Fluid Mechanics*, 48:397–404, 1971.

[20] P. Wesseling. The calculation of incompressible three-dimensional turbulent boundary layers. part 1: Formulation of a system of equations. Technical Report AT-69-01, Nationaal Lucht-En Ruimtevaartlaboratorium, Amsterdam, 1969.

[21] F. M. White. *Viscous Fluid Flow.* McGraw-Hill, New York, 1974.

[22] D. L. Whitfield, T. W. Swafford, and J. L. Jacocks. Calculation of turbulent boundary layers with separation and viscous-inviscid interaction. *AIAA Journal*, 19(10):1315–1322, Oct 1981.

[23] D.L. Whitfield, T.W. Swafford, and T.L. Donegan. An inverse integral computational method for compressible turbulent boundary layers. In W. Haase, editor, *Recent Contributions to Fluid Mechanics.* Springer-Verlag, 1982.